

FSGe: A fast and strongly-coupled 3D fluid-solid-growth interaction method

Martin R. Pfaller^a, Marcos Latorre^b, Erica L. Schwarz^{c,d}, Fannie M. Gerosa^a, Jason M. Szafron^a, Jay D. Humphrey^d,
Alison L. Marsden^a

^aDepartment of Pediatrics – Cardiology, Stanford University, Stanford, CA 94306, USA

^bCenter for Research and Innovation in Bioengineering, Universitat Politècnica de València, València, Spain

^cDepartment of Bioengineering, Stanford University, Stanford, CA 94306, USA

^dDepartment of Biomedical Engineering, Yale University, New Haven, CT 06520, USA

Abstract

Equilibrated fluid-solid-growth (FSGe) is a fast, open source, three-dimensional (3D) computational platform for simulating interactions between instantaneous hemodynamics and long-term vessel wall adaptation through growth and remodeling (G&R). Such models are crucial for capturing adaptations in health and disease and following clinical interventions. In traditional G&R models, this feedback is modeled through highly simplified fluid models, neglecting local variations in blood pressure and wall shear stress (WSS). FSGe overcomes these inherent limitations by strongly coupling the 3D Navier-Stokes equations for blood flow with a 3D equilibrated constrained mixture model (CMMe) for vascular tissue G&R. CMMe allows one to predict long-term evolved mechanobiological equilibria from an original homeostatic state at a computational cost equivalent to that of a standard hyperelastic material model. In illustrative computational examples, we focus on the development of a stable aortic aneurysm in a mouse model to highlight key differences in growth patterns and fluid-solid feedback between FSGe and solid-only G&R models. We show that FSGe is especially important in blood vessels with asymmetric stimuli. Simulation results reveal greater local variation in fluid-derived WSS than in intramural stress (IMS). Thus, differences between FSGe and G&R models became more pronounced with the growing influence of WSS relative to pressure. Future applications in highly localized disease processes, such as for lesion formation in atherosclerosis, can now include spatial and temporal variations of WSS.

1. Introduction

The intricate interaction between hemodynamics and growth (change in mass) and remodeling (change in microstructure) of a blood vessel plays a vital role in development, homeostasis, and disease progression [1]. The constrained mixture model (CMM) simulates the continuous deposition and degradation of tissue constituents [2, 3], often based on the concept of mechanical homeostasis, which is visualized in Figure 1. In this model of mechanobiological homeostasis, changes in vascular composition and properties stem from deviations in regulated variables from defined set points. These regulated variables primarily include intramural stress (IMS), σ_I , and wall shear stress (WSS), τ_w , which have consistently been found to be maintained at homeostatic values under physiologic conditions *in vivo* [4].

Hemodynamics \mathcal{F} are a crucial determinant of the biomechanical state of a blood vessel, characterized in part by its regulated variables. Solid mechanics \mathcal{S} within the vessel wall define blood vessel geometry and microstructure. Changes in the solid mechanics thus trigger changes in hemodynamics, \mathcal{F} , rendering the feedback loop a fluid-solid-growth interaction (FSG) problem. Most prior work considered either constant or reduced-order hemodynamics. The novelty of our work is a *strongly* coupled feedback between hemodynamics \mathcal{F} and solid mechanics \mathcal{S} in a fully three-dimensional (3D) framework based on the equilibrated constrained mixture model (CMMe) [5]. In the following, we review previous approaches in more detail and highlight the contributions of this work.

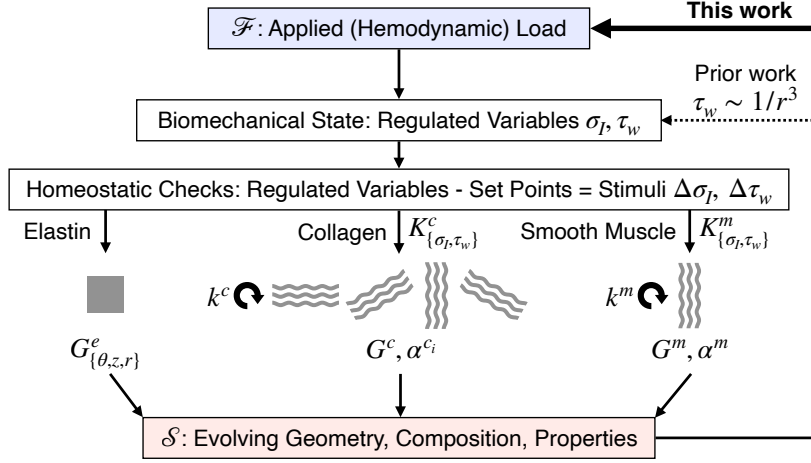


Figure 1: Negative feedback characteristics of mechanical homeostasis, including hemodynamics \mathcal{F} and solid mechanics \mathcal{S} . Stimuli consist of deviations of intramural stress, $\Delta\sigma_I$, and wall shear stress, $\Delta\tau_w$, from homeostatic set-point values. Tissue changes are modulated by gain factors $K_{\sigma_I}^\alpha$ and $K_{\tau_w}^\alpha$, which capture cell sensitivity to the particular stimulus. Growth and remodeling (G&R) are influenced further by degradation rate k^α , homeostatic prestretch G^α , and orientation angle α^α . In this work, tissue constituents α are elastin e , four collagen fiber families c , and smooth muscle m , which are visualized in Figure 2. Figure adapted from [3].

Hemodynamics *in vivo* typically include complex flow phenomena such as flow separation and recirculation induced by changes in cross-sectional area or bifurcations [6]. Consequently, pressure and WSS typically show a high spatial and temporal variation. Local hemodynamics can be quantified with computational fluid dynamics (CFD) or fluid-structure interaction (FSI) solutions [7]. However, the CMM commonly includes simplified assumptions for axial pressure gradient Δp and WSS τ_w based on Hagen–Poiseuille law [5]

$$\Delta p = \frac{8\mu l Q}{\pi r^4}, \quad \tau_w = \frac{4\mu Q}{\pi r^3}, \quad (1)$$

with dynamic blood viscosity μ , vessel length l and radius r , and bulk blood flow rate Q . These equations assume fully developed steady-state flow through a straight cylindrical tube with axisymmetric flow and zero radial and circumferential components, which is generally not upheld in *in vivo* settings.

Reference	Fluid	Solid	Stimuli	Coupling	Geometry
Figueroa et al. [8]	3D Navier-Stokes	Membrane CMM	pulsatile mean	weak	idealized
Sheidaei et al. [9]	3D Navier-Stokes	Membrane CMM	pulsatile mean	weak	<i>in vivo</i>
Watton et al. [10]	3D Navier-Stokes	3D hybrid	pulsatile mean	weak	<i>in vivo</i>
Grytsan et al. [11]	3D Navier-Stokes	3D hybrid	steady-state	weak	<i>in vivo</i>
Latorre et al. [12]	Control-volume	3D CMMe	steady-state	strong	idealized
Schwarz et al. [13]	3D Navier-Stokes	3D CMM	steady-state	strong	<i>in vivo</i>
<i>This work</i>	3D Navier-Stokes	3D CMMe	steady-state	strong	idealized

Table 1: Overview of some fluid-solid-growth interaction (FSG) interaction models.

The local interaction between hemodynamics and vessel growth and remodeling (G&R) mechanisms is crucial in numerous diseases and their treatments, as, for example, in tissue-engineered vascular grafts (TEVGs) [14, 15], vein graft adaptation and failure following coronary artery bypass graft surgery [16, 17], and in congenital heart patients with pulmonary disease [18, 19]. For an overview of G&R models, i.e., kinematic, constrained mixture model (CMM), and hybrid, see [20]. A non-comprehensive overview of similar fluid-solid-growth interaction models is given in Table 1. Figueroa et al. [8] developed a method that couples three-dimensional (3D) hemodynamics to a membrane model of the vessel wall. This theory is based on the *theory of small on large* [21], superimposing "small" deformations during the cardiac cycle upon "large" deformations due to G&R. The membrane wall formulation is

related to the coupled momentum method for fluid-structure interaction (FSI) in blood vessels [22]. The long-term G&R deformation is coupled to pulsatile hemodynamics, illustrated in an example of aneurysmal development. This approach was used in a patient-specific aneurysm geometry in Sheidaei et al. [9]. The work of Latorre et al. [12] couples 3D G&R with a simplified control-volume formulation of fluid dynamics. Pressure and wall shear stress (WSS) are derived from an axial node-based control-volume approach based on the Hagen-Poiseuille law (1) with additional pressure loss terms. For a more detailed discussion of reduced-order fluid dynamics, see Pfaller et al. [23]. Most recently, Schwarz et al. [13] coupled 3D CMM and 3D hemodynamics. While this constitutes the most detailed approach so far, it comes at high computational cost due to the need to integrate heredity integrals point-wise in full CMM.

Most FSG approaches reviewed above, except for Latorre et al. [12] and Schwarz et al. [13], employ weak coupling between fluid and solid G&R, also known as loose or weak coupling. Here, the fluid and solid domains are solved independently, with their solutions being exchanged only once in each load step. This approach assumes that the interaction between the fluid and solid is relatively weak, allowing for some degree of decoupling between the domains. Loose coupling is typically used for problems where the fluid and solid have a minor influence on each other or when computational efficiency is prioritized over solution accuracy. On the other hand, strong coupling schemes rely on an iterative procedure that ensures the convergence of fluid and solid solutions.

This work introduces an equilibrated fluid-solid-growth (FSGe) method to strongly couple 3D G&R based on the equilibrated constrained mixture model (CMMe) with 3D hemodynamics. Using CMMe greatly reduces the computational cost of evaluating the solid model and generally arrives at the desired model prediction in much fewer steps. In the following, we introduce the governing differential equations of the fluid and solid domains (Section 2). We then review computational techniques employed to solve the coupled fluid-solid problem (Section 3). In illustrative computational examples of an asymmetric aneurysm, we compare key differences between a solid-only G&R model and our FSGe formulation (Section 4). We close with a discussion of the results, limitations, and future perspectives (Section 5).

2. Governing equations of fluid and solid domains

As outlined in Figure 1, the FSGe model relies on the solution of fluid (2.1) and solid (2.2) mechanics, whose governing equations we briefly review in this section. Additionally, for completeness we introduce both the full CMM (2.2.1) and CMMe (2.2.2) G&R models. Both 3D fluid and solid were solved numerically in our open-source multi-physics solver `svFSIplus` [24], the C++ version of `svFSI` [25]; both solvers are released with the `SimVascular` project [26].

2.1. Fluid dynamics

We model blood flow in large vessels at high shear rates as a Newtonian fluid in the quasi-static fluid domain Ω^f within time scale T^f with the incompressible Navier-Stokes equations,

$$\nabla \cdot \boldsymbol{\sigma}^f(\mathbf{u}, p) = \rho \left[\frac{\partial \mathbf{u}}{\partial t} + (\mathbf{u} \cdot \nabla) \mathbf{u} \right], \quad \mathbf{x} \in \Omega^f, \quad t \in [0, T^f], \quad (2)$$

$$\nabla \cdot \mathbf{u} = 0, \quad \mathbf{x} \in \Omega^f, \quad t \in [0, T^f], \quad (3)$$

with density ρ , viscosity μ , and fluid Cauchy stress tensor $\boldsymbol{\sigma}^f = \mu(\nabla \mathbf{u} + \nabla \mathbf{u}^\top) - p\mathbf{I}$, where \mathbf{u} and p are fluid velocity and pressure, respectively. We prescribe boundary conditions

$$\begin{aligned} \mathbf{u}(\mathbf{x}, t) &= \mathbf{0}, & \mathbf{x} \in \Gamma_{\text{int}}, & \quad t \in [0, T^f], \\ \mathbf{u}(\mathbf{x}, t) &= \mathbf{u}_{\text{in}}(\mathbf{x}), & \mathbf{x} \in \Gamma_{\text{f,in}}, & \quad t \in [0, T^f], \\ \mathbf{n} \cdot \boldsymbol{\sigma}^f(\mathbf{x}, t) \cdot \mathbf{n} &= p_{\text{out}}, & \mathbf{x} \in \Gamma_{\text{f,out}}, & \quad t \in [0, T^f], \end{aligned}$$

with a no-slip boundary condition at the fluid-solid interface Γ_{int} , constant quadratic inflow profile \mathbf{u}_{in} at the inlet $\Gamma_{\text{f,in}}$, and constant outlet pressure p_{out} at the outlet $\Gamma_{\text{f,out}}$ with normal \mathbf{n} . The initial conditions are

$$\begin{aligned} \mathbf{u}(\mathbf{x}, t = 0) &= \mathbf{u}_0(\mathbf{x}), & \mathbf{x} \in \Omega^f, \\ p(\mathbf{x}, t = 0) &= p_0(\mathbf{x}), & \mathbf{x} \in \Omega^f, \end{aligned}$$

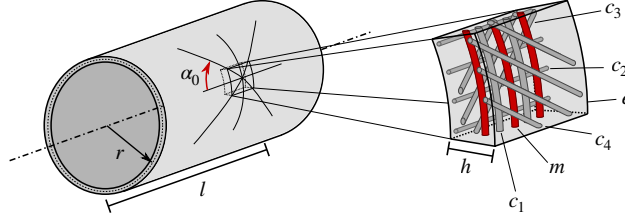


Figure 2: Blood vessel with length l , radius r , and thickness h . Its constituents are elastin e (isotropic), smooth muscle m (red, circumferential), and four collagen fiber families c_i (circumferential, axial, diagonal angle α_0). Image created by Sebastian L. Fuchs and licensed under the Creative Commons Attribution 4.0 International License.

with initial velocity field \mathbf{u}_0 and initial pressure field p_0 . See Esmaily Moghadam et al. [27, 28] for details on the P1-P1 variational multiscale finite element solution of the Navier-Stokes equations.

2.2. Solid growth and remodeling

We follow the classic approach of finite strain theory to model the vessel wall displacement, $\mathbf{d} = \mathbf{x} - \mathbf{X}$, with reference position \mathbf{X} and current position \mathbf{x} . We calculate the deformation gradient \mathbf{F} , the Jacobian J , and the right Cauchy–Green tensor \mathbf{C} as

$$\mathbf{F} = \frac{\partial \mathbf{x}}{\partial \mathbf{X}}, \quad J = \det \mathbf{F}, \quad \mathbf{C} = \mathbf{F}^T \mathbf{F}.$$

The balance of linear momentum in the case of negligible inertial loads [29] in the solid domain Ω^s yields the quasi-static problem

$$\nabla \cdot \boldsymbol{\sigma}^s = \mathbf{0}, \quad \mathbf{x} \in \Omega^s, \quad t \in [0, T^s], \quad (4)$$

with solid stress tensor $\boldsymbol{\sigma}^s$ provided constitutively by the G&R material and its solid time scale T^s . We prescribe boundary conditions

$$\begin{aligned} d_a(\mathbf{x}, t) &= 0, & \mathbf{x} \in \Gamma_{\text{cap}}, & \quad t \in [0, T^s], \\ \boldsymbol{\sigma}^s(\mathbf{x}, t) \cdot \mathbf{n}(\mathbf{x}, t) &= k \mathbf{d}(\mathbf{x}, t), & \mathbf{x} \in \Gamma_{\text{out}}, & \quad t \in [0, T^s], \end{aligned}$$

with zero Dirichlet boundary conditions in axial direction z at the caps of the blood vessel Γ_{cap} and external tissue support with outward normal \mathbf{n} and stiffness k [30]. Note that our external tissue support does not include viscous damping since G&R is a quasi-static process. The initial condition is

$$\mathbf{d}(\mathbf{x}, t = 0) = \mathbf{0}, \quad \mathbf{x} \in \Omega^s,$$

We use a G&R constitutive law to relate deformation \mathbf{F} to stresses $\boldsymbol{\sigma}^f$. In the following, we briefly review the full CMM and the CMMe. The CMM has been diversely applied, e.g., in altered flow and pressure conditions [31], abdominal [32] and thoracic [33] aortic aneurysms, vein grafts [34], or tissue-engineered vascular grafts [35]. However, due to its computational complexity, there are only limited implementations in three dimensions [36, 37]. In this work, we use the fast, rate-independent CMMe method that directly predicts the long-term evolved solution that is in mechanobiological equilibrium [38]. This material model had been previously implemented in the open-source finite element solver FEBio [39], with computational costs comparable to hyperelastic materials [5]. Prior work relied on constant-pressure models [5, 33, 40] and control-volume hemodynamics [12]. We briefly introduce the CMM in Section 2.2.1 and outline the CMMe in Section 2.2.2 but refer interested readers to the original publications.

2.2.1. Constrained Mixture Model

The CMM assumes that structurally significant constituents α with individual reference configurations, material properties, mass balance relations, and turnover rates are constrained to move together. The mass production per unit

volume at G&R time $\tau \in [0, s]$, where s is the current G&R time and τ is an intermediate time at which constituents are deposited, is expressed as

$$m^\alpha(\tau) = m_o^\alpha \Upsilon^\alpha(\tau),$$

using an original rate $m_o^\alpha > 0$ that is modulated by a stimulus function, as, for example,

$$\Upsilon^\alpha(\tau) = 1 + K_\sigma^\alpha \Delta\sigma_I(\tau) - K_\tau^\alpha \Delta\tau_w(\tau_w), \quad (5)$$

with gain parameters $K_i^\alpha > 0$ controlling the sensitivity to stress deviations $\Delta\sigma_I$ and $\Delta\tau_w$, respectively. We define these stimuli as

$$\Delta\sigma_I(\tau) = \frac{\sigma_I(\tau)}{\sigma_{Io}} - 1, \quad \Delta\tau_w(\tau) = \frac{\tau_w(\tau)}{\tau_{wo}} - 1. \quad (6)$$

governed by changes in intramural stress (IMS) σ_I (induced by pressure and axial force) and WSS τ_w (induced by blood flow) from homeostatic set points σ_{Io} and τ_{wo} , respectively. The constituent removal between deposition times τ and current time s is modeled by an exponential decay

$$q^\alpha(s, \tau) = \exp\left(-\int_\tau^s k^\alpha(t) dt\right), \quad k^\alpha(t) = k_o^\alpha \left[1 + K^\alpha \Delta\sigma^2(t)\right],$$

where k^α is a rate parameter with homeostatic value k_o^α , and $K^\alpha > 0$ is a gain parameter for IMS deviation. We can express the mass density per current volume of each constituent ρ_R^α by

$$\rho^\alpha(s) = \int_{-\infty}^s m^\alpha(\tau) q^\alpha(s, \tau) d\tau, \quad (7)$$

where m^α is the mass density production rate. The constituent-specific elastic strain energy density functions \hat{W}^α for elastin e , collagen c , and smooth muscle m are characterized by the neo-Hookean and Fung-type exponential relations as

$$\hat{W}^e = c^e (I_1^e - 3), \quad \hat{W}^{m,c} = \frac{c_1^{m,c}}{4c_2^{m,c}} \left[\exp\left(c_2^{m,c} (I_4^{m,c} - 1)^2\right) - 1 \right], \quad (8)$$

where $c^e, c_1^{m,c}, c_2^{m,c}$ are material parameters and $I_1^e, I_4^{m,c}$ are constituent-specific measures of deformation that are invariant to the coordinate system used. The constituents are visualized in Figure 2. Collagen fibers are further classified into circumferentially, axially, and diagonally oriented (at angle α_0) populations with fractions β_θ, β_z , and β_d , respectively. The constituent relations (8) are evaluated as $\hat{W}^\alpha(\mathbf{F}_{n(\tau)}^\alpha(s))$ with the deformation gradient

$$\mathbf{F}_{n(\tau)}^\alpha(s) = \mathbf{F}(s) \mathbf{F}^{-1}(\tau) \mathbf{G}^\alpha(\tau), \quad (9)$$

where \mathbf{G}^α is the constituent-specific preferred homeostatic pre-stretch, which can be reduced to the scalars $G^{m,c}$ for smooth muscle cells and collagen fibers. The elastin prestretch tensor \mathbf{G}^e is characterized by the components $G_{\theta,r,z}^e$. We obtain the total strain energy density

$$W(s) = \sum_\alpha W^\alpha(s), \quad W^\alpha(s) = \int_{-\infty}^s \frac{m^\alpha(\tau) q^\alpha(s, \tau)}{\rho(s)} \hat{W}_{n(\tau)}^\alpha(s) d\tau.$$

The constituent-specific mass fraction ϕ^α at time s is defined as

$$\phi^\alpha(s) = \frac{\rho^\alpha(s)}{\rho(s)}.$$

2.2.2. Equilibrated Constrained Mixture Model

The CMME directly predicts the long-term evolved state in mechanical and biological equilibrium, i.e., at $s \rightarrow \infty$, where production again balances removal. Note that CMME can still be used to predict transient G&R phenomena as long as the process is considered to be quasi-equilibrated, similar to classical problems in mechanics of quasi-equilibrated problems. Toward this end, it is assumed that the imposed perturbations to the homeostatic state are slow relative to the adaptive G&R process. For this purpose, the G&R process is broken up into several quasi-static *load steps* where perturbations are applied in increments. This rate-independent approach does not require computing hereditary integrals (7), thus drastically lowering the computational demand. In CMME, the stimulus function in Equation (5) reduces to

$$\Upsilon_h^\alpha(\Delta\sigma_{Ih}, \Delta\tau_{wh}) = 1, \quad (10)$$

depending on the equilibrated stimulus functions that can be simplified from (6) as

$$\Delta\sigma_{Ih} = \frac{\sigma_{Ih}}{\sigma_{Io}} - 1, \quad \Delta\tau_{wh} = \frac{\tau_{wh}}{\tau_{wo}} - 1, \quad (11)$$

comparing the evolved equilibrium h to the original homeostasis o , hence eliminating the time-dependency on τ . All values with index o are determined at a hyperelastic pre-loading stage ($t = 0$), followed by the G&R stage h to determine the long-term evolved variables in mechanobiological equilibrium ($t > 0$). The equilibrated stimulus function yields

$$\Delta\sigma_{Ih} = K_{\tau\sigma} \Delta\tau_{wh}, \quad K_{\tau\sigma} = \frac{K_\tau^\alpha}{K_\sigma^\alpha} \geq 0 \quad \forall \alpha, \quad \eta = \frac{K^m}{K^c}, \quad (12)$$

with a single shear-to-intramural gain ratio $K_{\tau\sigma}$ for all constituents α and smooth muscle-to-collagen turnover ratio η . Note that for $K_{\tau\sigma} = 0$ and $K_{\tau\sigma} \rightarrow \infty$ the blood vessel perfectly maintains IMS σ_{Ih} and WSS τ_{wh} , respectively. We obtain the solid Cauchy stress

$$\boldsymbol{\sigma}^s = \boldsymbol{\sigma}^x - p_h \mathbf{I}, \quad \boldsymbol{\sigma}^x = \sum_{\alpha}^{e.c.m} \phi_h^\alpha \hat{\boldsymbol{\sigma}}_h^\alpha, \quad (13)$$

where $\hat{\boldsymbol{\sigma}}_h^\alpha$ are the equilibrated constituent-specific Cauchy stresses, $\boldsymbol{\sigma}^x$ is the mixture stress, and p_h is the equilibrated Lagrange multiplier that enforces mechanobiological equilibrium. We define the IMS invariant throughout this work as

$$\sigma_I = \frac{\text{tr } \boldsymbol{\sigma}^s}{3}, \quad (14)$$

calculated from the solid stress tensor $\boldsymbol{\sigma}^s$. We can now express the Lagrange multiplier, using (12), (13), and (14), as

$$p_h = \sigma_{Ih}^x - \sigma_{Io} \left[1 + K_{\tau\sigma} \left(\frac{\tau_{wh}}{\tau_{wo}} - 1 \right) \right], \quad \sigma_{Ih}^x = \frac{\text{tr } \boldsymbol{\sigma}^x}{3}. \quad (15)$$

The invariant σ_{Ih}^x can be explicitly calculated from the mixture stress $\boldsymbol{\sigma}^x$. The original homeostatic IMS σ_{Io} is stored locally from the pre-loading stage. Note that the tangential stiffness matrix of the CMME material model only has minor symmetries, no major symmetries. This can pose challenges for iterative linear solvers and their preconditioners. We thus use the distributed memory sparse direct linear solver MUMPS [41] within the PETSc suite [42].

3. Fluid-solid-growth coupling

In classic FSI, the solid material behavior is purely determined by an *elastic* response to boundary conditions and interface conditions at the fluid-solid interface Γ_{int} . In contrast, the CMME material behavior is characterized by a *long-term* mechanobiological response to mechanical stimuli. In this section, we first highlight key similarities and

differences between FSI and FSGe problems and then derive a robust coupling scheme. WSS is a crucial stimulus in the models used in this work. Its local calculation is a key difference between purely solid G&R models and FSGe:

$$\text{G\&R: } \Delta\tau_{wh} \approx \left(\frac{a_h}{a_o}\right)^{-3} - 1 \approx \left[\frac{r_o}{a_o} \lambda_\theta - \left(\frac{r_o}{a_o} - 1\right) \lambda_r\right]^{-3} - 1, \quad \lambda_i = \sqrt{\mathbf{C}_h : \mathbf{e}_i \otimes \mathbf{e}_i}. \quad (16)$$

$$\text{FSGe: } \Delta\tau_{wh} = \frac{\|\boldsymbol{\tau}_{wh}\|}{\|\boldsymbol{\tau}_{wo}\|} - 1. \quad (17)$$

In the G&R model, local WSS is approximated with the Poiseuille flow-derived WSS (1). The evolved local inner radius a_h of the blood vessel is approximated locally at each Gauß point of the finite elements. The approximation uses the radial coordinate r_o and inner radius a_o in original homeostasis as well as the evolved local circumferential stretch λ_θ and radial stretch λ_r with unit vectors \mathbf{e}_i [5]. In the FSGe model, we use the magnitude of the local WSS vector $\boldsymbol{\tau}_w$ extracted at the fluid-solid interface from a steady-state fluid solution. In response to local changes in WSS, the endothelium alters its production of vasoactive molecules that rapidly diffuse into the wall and cause vascular smooth muscle cell relaxation or contraction [43]. Instead of solving the diffusion equation, this work assumes that the WSS stimulus at the interface Γ_{int} effects each radial location equally within the vessel wall. Thus, the FSGe model is coupled via

$$\boldsymbol{\sigma}^s := \boldsymbol{\sigma}^s(\boldsymbol{\tau}_w) = \boldsymbol{\sigma}^s(\boldsymbol{\sigma}_{\Gamma_{\text{int}}}^f), \quad \mathbf{x} \in \Omega^s, \quad (18)$$

to the solid stress tensor $\boldsymbol{\sigma}^s$. Modeling the effect of vasoactive molecules, at every location in the vessel the solid stress $\boldsymbol{\sigma}^s$ depends on WSS $\boldsymbol{\tau}_w$, which, in turn, depends on the fluid stress tensor $\boldsymbol{\sigma}_{\Gamma_{\text{int}}}^f$ at the interface Γ_{int} . This interaction differs from classic FSI problems, where fluid and solid are only coupled at the interface. In FSGe, the fluid-solid interface is coupled to the whole solid volume. Furthermore, in blood flow, WSS $\boldsymbol{\tau}_w$ is typically five orders of magnitude smaller than the IMS σ_I . Thus, WSS has a negligible *mechanical* influence in vascular FSI models, but, depending on the gain ratio $K_{\tau\sigma}$, a large *biological* influence in the FSGe model. Also, solid G&R takes place on a time scale $T^s \gg T^f$ of weeks or months, which is much larger than the fluid dynamics time scale T^f . Thus, we can derive the interface velocity from the interface displacements \mathbf{d} as

$$\mathbf{u}_{\Gamma_{\text{int}}} = \frac{\partial \mathbf{d}}{\partial t^s} \approx \mathbf{0}, \quad \mathbf{x} \in \Gamma_{\text{int}}, \quad (19)$$

which differs from the typical FSI condition that non-zero fluid and solid velocities must match at the interface. The interface condition (19) is equivalent to a no-slip condition in a rigid-wall fluid simulation. The traction interface condition

$$\boldsymbol{\sigma}_{\Gamma_{\text{int}}}^s \cdot \mathbf{n} = \boldsymbol{\sigma}_{\Gamma_{\text{int}}}^f \cdot \mathbf{n}, \quad \mathbf{x} \in \Gamma_{\text{int}}, \quad (20)$$

is identical to most FSI problems, with interface normal vector \mathbf{n} . While blood pressure is typically assumed to be constant in purely solid G&R models, the FSGe couples the normal components of local solid and fluid stress tensors, $\boldsymbol{\sigma}_{\Gamma_{\text{int}}}^s$ and $\boldsymbol{\sigma}_{\Gamma_{\text{int}}}^f$, respectively, which spatially vary according to the solution of the Navier-Stokes equations.

The choice of coupling scheme is crucial for the robustness and accuracy of the FSGe model. For a comprehensive review of FSI coupling approaches, we refer to Hou et al. [44]. We refer to Degroote [45] for an extensive discussion of partitioned fluid-structure coupling approaches and reuse some of the notations in this section. The FSGe model proposed in this work is available open-source in the Python coupling code svFSGe [46]. In the remainder of this section, we briefly review key differences between *monolithic* (3.1) and *partitioned* (3.2) coupling schemes for their use in FSGe. The monolithic approach simultaneously solves the space- and time-discretized fluid and solid fields. In contrast, the partitioned approach solves fluid and solid fields separately and can be implemented with either weak (3.2.1) or strong (3.2.2) coupling.

3.1. Monolithic coupling

Let \mathbf{f} and \mathbf{s} denote the fluid and solid residual, respectively. The vector \mathbf{U} represents the discrete fluid variables velocity and pressure; the vector \mathbf{D} represents the discrete solid displacements. The monolithic FSI problem is then given by

$$\begin{cases} \mathbf{f}(\mathbf{U}, \mathbf{D}) = \mathbf{0} \\ \mathbf{s}(\mathbf{U}, \mathbf{D}) = \mathbf{0} \end{cases}. \quad (21)$$

This system is commonly solved with the Newton-Raphson method. The update for fluid and solid increments, $\Delta\mathbf{U}$ and $\Delta\mathbf{D}$, respectively in iteration k at a load step t becomes

$$\begin{bmatrix} \partial_{\mathbf{U}} \mathbf{f} & \partial_{\mathbf{D}} \mathbf{f} \\ \partial_{\mathbf{U}} \mathbf{s} & \partial_{\mathbf{D}} \mathbf{s} \end{bmatrix}_{t,k} \begin{bmatrix} \Delta\mathbf{U} \\ \Delta\mathbf{D} \end{bmatrix}_{t,k+1} = - \begin{bmatrix} \mathbf{f} \\ \mathbf{s} \end{bmatrix}_{t,k}, \quad (22)$$

where $\partial_{\mathbf{U}} \mathbf{f}$ denotes the partial derivative of \mathbf{f} with respect to \mathbf{U} . All blocks in Equation (22) are treated in the same mathematical framework and implemented in `svFSIplus`. For FSI problems, the advantages of monolithic coupling can be faster convergence and higher accuracy than the partitioned approach. However, it may require more computational resources and a more intrusive software implementation. Independent of these challenges, we found a monolithic coupling approach to be intractable for an FSGe problem. Solving Equation (22) requires solving both fluid and solid fields with the same time step size, typically $T_{\text{FSI}} \sim 1$ ms or below in cardiovascular FSI problems [47]. However, as discussed in Section 3, solid G&R takes place over a much longer time scale than blood flow fluid dynamics. In fact, the CMME returns the mechanobiological equilibrated G&R response after an *infinitely* long period $s \rightarrow \infty$ at every load step t . This limit renders solving Equation 22 with a uniform fluid-solid time step size intractable, and we, therefore, chose a partitioned scheme for FSGe. Note that we refer to t throughout this work as a quasi-static G&R *load step* opposed to a *time step* in a dynamic problem. All load steps represent a long-term equilibrium at $s \rightarrow \infty$, typically for different insult severities.

3.2. Partitioned coupling

In partitioned FSI, fluid field \mathcal{F} and solid field \mathcal{S} solve for interface traction \mathbf{u} and interface displacements \mathbf{d} , respectively so that

$$\mathbf{u} = \mathcal{F}(\mathbf{d}), \quad (23)$$

$$\mathbf{d} = \mathcal{S}(\mathbf{u}). \quad (24)$$

In the fluid field \mathcal{F} , in addition to solving blood flow dynamics (Section 2.1), we apply a deformation to the computational grid of Ω^f to avoid excessive fluid mesh distortion. This is similar to the arbitrary Lagrangian-Eulerian (ALE) formulation typically employed in FSI problems where an arbitrary grid velocity is applied. However, due to (19), the mesh deformation is quasi-static in FSGe. In the FSGe model, we apply an interface mesh deformation \mathbf{d}_{int} and solve a linear elasticity problem to solve for the fluid mesh deformation

$$\mathbf{K} \cdot \mathbf{d}_f = \mathbf{0}, \quad \text{with } \mathbf{d}_f = \mathbf{d}_{\text{int}} \text{ on } \Gamma_{\text{int}}, \quad (25)$$

with a stiffness matrix \mathbf{K} . Inspired by Degroote [45], we outline the steps within the fluid and solid solvers in Algorithms 1 and 2, respectively. Partitioned FSI offers the advantage of reusing and combining existing fluid and solid solvers with solution techniques targeted to the respective domain. Note that while independent solvers could be used for \mathcal{F} and \mathcal{S} , we use our open-source multi-physics solver `svFSIplus` for both [25]. Crucially, this allows us to natively split both time scales arising in the FSGe problem. We thus focus on a partitioned coupling approach for the remainder of this work.

Algorithm 1 \mathcal{F} : Steady-state fluid

- 1: Apply interface displacement \mathbf{d}
 - 2: Deform the fluid domain (25)
 - 3: Solve for fluid variables \mathbf{U}
 - 4: Extract interface traction \mathbf{u}
-

Algorithm 2 \mathcal{S} : Quasi-static solid

- 1: Apply interface traction \mathbf{u}
 - 2: Propagate WSS through solid domain
 - 3: Solve for solid variables \mathbf{D}
 - 4: Extract interface displacement \mathbf{d}
-

Note that in comparison to a classic FSI problem, in FSGe we additionally need to radially propagate the effects of the WSS at the interface throughout the thickness of the blood vessel in the solid domain (line 2 in Algorithm 2) as discussed in Section 2.2. In a cylindrical reference domain with a structured solid grid, this can be easily facilitated with a cylindrical coordinate system. A radial coordinate can be defined in patient-specific geometries, e.g., by solving a diffusion problem commonly used in cardiac geometries [48].

3.2.1. Weak coupling

The group of partitioned FSI coupling schemes can be further split into implicit (or *strong*), semi-implicit, and explicit (or *weak*) schemes [49]. As Section 1 outlines, most previous FSG approaches used weak coupling. Algorithm 3 illustrates the most basic case of a serial staggered weak coupling scheme. Here, the fluid solution is updated once in every load step t based on the solid solution \mathbf{d}_{t-1} from the previous load step. The updated fluid solution is then input to update the solid solution \mathbf{d}_t . For FSGe, this weak coupling method is unstable for $K_{\tau\sigma} > 0$ and is thus not further pursued in this work. Although weakly coupled FSI problems can sometimes be stabilized by reducing the time step size, this strategy is not possible in FSGe. While an applied stimulus can be spread over more load steps, the time-independent solid CMMe model always yields a long-term evolved equilibrium at $s \rightarrow \infty$.

Algorithm 3 Weak coupling scheme

```

1:  $\mathbf{d}_0 = \mathbf{0}$ ,  $t = 0$ 
2: do
3:    $t++$ 
4:    $\mathbf{d}_t = \mathcal{S} \circ \mathcal{F}(\mathbf{d}_{t-1})$ 
5: while  $t \leq t_{\max}$ 

```

3.2.2. Strong coupling

Strong coupling schemes enforce an equilibrium between fluid and solid fields in every load step, which requires an additional iteration loop. Strong coupling is essential to solve the FSGe problem when there is a strong interaction between fluid and solid, which is the case for $K_{\tau\sigma} > 0$, that is, when the solid G&R material depends on local WSS. We control the convergence towards an equilibrium in coupling iterations k at every load step t with the displacement residual

$$\mathbf{r}_{t,k} = \tilde{\mathbf{d}}_{t,k} - \mathbf{d}_{t,k}, \quad (26)$$

In the following, $\tilde{\mathbf{d}}_{t,k}$ denotes the output of a subsequent fluid-solid solve

$$\tilde{\mathbf{d}}_{t,k} = \mathcal{S} \circ \mathcal{F}(\mathbf{d}_{t,k}), \quad (27)$$

in contrast to the input $\mathbf{d}_{t,k}$. Equilibrium between fluid and solid is achieved when the relative displacement error norm

$$\frac{\|\mathbf{r}_{t,k}\|_2}{\|\mathbf{d}_{t,k}\|_2} < \epsilon_0, \quad (28)$$

is smaller than a given tolerance ϵ_0 . The most basic form of strong coupling is the Gauß-Seidel iteration scheme depicted in line 8 of Algorithm 4. Here, fluid mesh deformation, fluid, and solid are executed sequentially, and we use the output from the previous coupling iteration as the input for the current iteration:

$$\mathbf{d}_{t,k} = \tilde{\mathbf{d}}_{t,k-1}. \quad (29)$$

Gauß-Seidel schemes typically converge slowly or might not converge at all [45]. A straightforward approach to stabilize the Gauß-Seidel scheme is to introduce static relaxation

$$\mathbf{d}_{t,k} = \omega \tilde{\mathbf{d}}_{t,k-1} + (1 - \omega) \mathbf{d}_{t,k-1}, \quad 0 < \omega \leq 1, \quad (30)$$

with a static relaxation parameter ω , which reduces to the Gauß-Seidel scheme (29) for $\omega = 1$. While usually improving numerical stability for $0 < \omega < 1$, this coupling scheme typically converges slowly and highly depends on the choice of the relaxation parameter ω . A much more efficient scheme is obtained by dynamically choosing ω_k in each iteration k through Aitken relaxation [50, 51]:

$$\omega_k = -\omega_{k-1} \frac{\mathbf{r}_{k-1} \cdot \Delta \mathbf{r}_k}{\|\Delta \mathbf{r}_k\|_2}, \quad \text{with } \Delta \mathbf{r}_k = \mathbf{r}_k - \mathbf{r}_{k-1}. \quad (31)$$

While easy to implement, Aitken relaxation can use only information from one previous coupling iteration and is thus limited in its potential to introduce stabilization to the coupling scheme. The interface quasi-Newton with inverse

Jacobian from a least-squares model (IQN-ILS) can use information from up to q previous coupling iterations [45, 52]. It is based on applying the Newton-Raphson method to solve the equation $\mathbf{r}_t = \mathbf{0}$, which yields

$$\mathbf{d}_{t,k} = \tilde{\mathbf{d}}_{t,k-1} - \left(\frac{\partial \mathbf{r}}{\partial \tilde{\mathbf{d}}} \Big|_{t,k-1} \right)^{-1} \mathbf{r}_{k-1}. \quad (32)$$

However, the Jacobian matrix $\partial \mathbf{r} / \partial \tilde{\mathbf{d}}$ is not known explicitly, and an approximation with finite differences would require several additional solver evaluations. In IQN-ILS, the Jacobian is approximated from a linear combination of known previous displacements, computing the input displacements as

$$\mathbf{d}_{t,k} = \tilde{\mathbf{d}}_{t,k-1} + \mathbf{W}\mathbf{c}, \quad \text{with } \mathbf{W} = [\Delta \tilde{\mathbf{d}}_{k-1}, \Delta \tilde{\mathbf{d}}_{k-2}, \dots], \quad \Delta \tilde{\mathbf{d}}_{k-1} = \tilde{\mathbf{d}}_k - \tilde{\mathbf{d}}_{k-1}, \quad (33)$$

with coefficient vector \mathbf{c} which we obtain by solving the least squares problem

$$\min_{\mathbf{c}} \|\mathbf{V}\mathbf{c} + \mathbf{r}_k\|_2, \quad \text{with } \mathbf{V} = [\Delta \mathbf{r}_{k-1}, \Delta \mathbf{r}_{k-2}, \dots]. \quad (34)$$

This minimization problem is solved using the QR-decomposition $\mathbf{QR} = \mathbf{V}$. The matrices \mathbf{V} and \mathbf{W} are updated in every coupling iteration k and truncated to contain a maximum of q entries. We reuse information from previous load steps in \mathbf{V} and \mathbf{W} but never calculate increments across load steps. Furthermore, filtering ensures that linearly dependent columns i_ϵ are excluded from \mathbf{V} and \mathbf{W} when $\mathbf{R}_{ii} < \epsilon_{QR}$. The IQN-ILS approach is summarized in Algorithm 6.

Algorithm 4 Strongly coupled FSGe

```

1:  $\mathbf{V} = \emptyset, \mathbf{W} = \emptyset, t = 0$ 
2: do
3:    $k = 0$ 
4:    $\mathbf{d}_{t,0}$  from Algorithm 5
5:   do
6:      $k++$ 
7:     if  $t = 0$  then
8:        $\mathbf{d}_{t,k} = \tilde{\mathbf{d}}_{t,k-1}$ 
9:     else if  $(k = 1)$  or  $(t = 1$  and  $k \leq 5)$  then
10:       $\mathbf{d}_{t,k} = \omega \tilde{\mathbf{d}}_{t,k-1} + (1 - \omega) \mathbf{d}_{t,k-1}$ 
11:     else
12:       $\mathbf{d}_{t,k}$  from Algorithm 6
13:     end if
14:      $\tilde{\mathbf{d}}_{t,k} = \mathcal{S} \circ \mathcal{F}(\mathbf{d}_{t,k})$ 
15:      $\mathbf{r}_{t,k} = \tilde{\mathbf{d}}_{t,k} - \mathbf{d}_{t,k}$ 
16:     while  $\|\mathbf{r}_{t,k}\|_2 / \|\tilde{\mathbf{d}}_{t,k}\|_2 > \epsilon_0$ 
17:        $t++$ 
18:     while  $t \leq t_{\max}$ 

```

Algorithm 5 Polynomial predictor

```

1: if  $t = 0$  then
2:    $\mathbf{d}_{t,0} = \mathbf{d}_0$ 
3: else
4:    $\mathbf{d}_{t,0} = 2\mathbf{d}_1 - \mathbf{d}_0$ 
5: end if

```

Algorithm 6 IQN-ILS

```

1:  $\mathbf{V} = (\mathbf{r}_{t,k} - \mathbf{r}_{t,k-1}, \mathbf{V})$ 
2:  $\mathbf{W} = (\tilde{\mathbf{d}}_{t,k} - \tilde{\mathbf{d}}_{t,k-1}, \mathbf{W})$ 
3:  $\mathbf{V} = \mathbf{V} \setminus \mathbf{V}_{i>q}, \mathbf{W} = \mathbf{W} \setminus \mathbf{W}_{i>q}$ 
4: do
5:    $\mathbf{QR} = \mathbf{V}$ 
6:    $i_\epsilon = \arg_i (|\mathbf{R}_{ii}| < \epsilon_{QR})$ 
7:    $\mathbf{V} = \mathbf{V} \setminus \mathbf{V}_{i_\epsilon}, \mathbf{W} = \mathbf{W} \setminus \mathbf{W}_{i_\epsilon}$ 
8:   while  $i_\epsilon \neq \emptyset$ 
9:      $\mathbf{c} = \mathbf{R}^{-1} \mathbf{b}$  with  $\mathbf{b} = -\mathbf{R}^{-T} (\mathbf{V} \mathbf{r}_{t,k})$ 
10:     $\mathbf{d}_{t,k} = \tilde{\mathbf{d}}_{t,k-1} + \mathbf{W}\mathbf{c}$ 

```

The strongly coupled FSGe method is outlined in Algorithm 4. We use a Gauß-Seidel scheme exclusively at $t = 0$ for the pre-loading stage in CMMe [5] in line 8. Here, the displacements are negligibly small, and there is only weak coupling as pre-loading does not depend on local WSS. The G&R stage in CMMe at $t > 0$ requires the more robust IQN-ILS coupling approach in line 12. Note that the performance of the algorithm also crucially depends on an accurate prediction of displacements $\mathbf{d}_{t,0}$ at the beginning of each load step. If a previous load step is available, we use the linear predictor in Algorithm 5. Further, note that at the beginning of each coupling iteration $k = 1$, we obtain input displacements $\mathbf{d}_{t,k}$ from a static relaxation step (30). Similarly, we use static relaxation for the first five coupling iterations at $t = 1$, i.e., the first G&R load step, to collect an initial number of iterations for IQN-ILS.

4. Illustrative computational examples

This section compares our equilibrated fluid-solid-growth (FSGe) model to a purely solid growth and remodeling (G&R) model. As an illustrative example, we focus on the growth of an aortic aneurysm in a mouse. Aortic aneurysms

have been studied in prior work using the equilibrated constrained mixture model (CMMe) [5, 33] and a prior fluid-solid-growth coupling method [8]. Given the inherently large deformation in aortic aneurysms, they locally alter blood flow [53] and are thus a good example to demonstrate differences between solid G&R and FSGe and a good starting step for more complex *in vivo* flow patterns in future research.

Solid G&R parameters [5]		
Constituents	e, m, c	elastin, smooth muscle, collagen
Inner radius, thickness, length	a_o, h_o, l_o	0.647 mm, 0.04 mm, 15 mm
Mass fractions	$\phi_o^e, \phi_o^m, \phi_o^c$	0.34, 0.33, 0.33
Collagen orientation fractions	$\beta_\theta, \beta_z, \beta_d$	0.056, 0.067, 0.877
Diagonal collagen orientation	α_0	29.9°
Elastin stiffness	c_o^e	89.71 kPa
Smooth muscle parameters	c_1^m, c_2^m	261.4 kPa, 0.24
Collagen parameters	c_1^c, c_2^c	234.9 kPa, 4.08
Deposition stretches	$G_\theta^e, G_z^e, G_r^e, G^m, G^c$	1.90, 1.62, 1/($G_\theta^e G_z^e$), 1.20, 1.25
Smooth muscle-to-collagen turnover ratio	η	1.0
Shear-to-intramural gain ratio	$K_{\tau\sigma,o}$	{0.0, 0.2, 0.4, 0.6, 0.8, 1.0}
External tissue support stiffness	k	2.0 kPa/mm
Aneurysm parameters		
Circumferential extent	θ_{od}	0.55 π
Circumferential decay	v_θ	6
Axial extent	z_{od}	$l_o/4$
Axial decay	v_z	2
Maximum elastin degradation	φ_{hm}^e	0.7
Fluid parameters		
Maximum inflow velocity	u_{in}	1000 mm/s
Outlet pressure [5]	p_{out}	104.9 mmHg
Dynamic viscosity	μ	$4.0 \cdot 10^{-6}$ kg/mm/s
Density	ρ	$1.06 \cdot 10^{-6}$ kg/mm ³
Numerical parameters		
Number of elements	$n_\theta \times n_r \times n_z$	$64 \times 1 \times 40$
Number of G&R load steps [5]	t_{max}	10
Coupling tolerance	ϵ_0	10^{-3}
Static relaxation parameter	ω	0.1
IQN-ILS filtering tolerance	$\epsilon_{IQN-ILS}$	10^{-1}
IQN-ILS number of old iterations	q	20

Table 2: Parameters used in all computational examples in this work.

For an overview of all parameters, see Table 2, where the solid G&R parameters are taken from Latorre and Humphrey [5]. All parameters in the G&R model are identical to the FSGe model, with the FSGe having additional fluid and coupling parameters. The inflow velocity u_{in} was chosen as an upper bound for systolic velocities observed in mouse aortas [54]. Aneurysmal growth is associated with elastin degradation, modeled here by decreasing elastin stiffness [55], i.e., $c_h^e \rightarrow 0$, and loss of mechanosensation, i.e., $K_{\tau\sigma,h} \rightarrow 0$ [56]. We apply a spatial insult profile to trigger asymmetric aneurysmal growth,

$$c_h^e(\theta, z, t) = c_o^e [1 - \varphi_{hm}^e f(\theta, z, t)], \quad (35)$$

$$K_{\tau\sigma,h}(\theta, z, t) = K_{\tau\sigma,o} [1 - f(\theta, z, t)], \quad (36)$$

reducing long-term evolved elastin stiffness c_h^e and gain ratio $K_{\tau\sigma,h}$ with the spatial and temporal factor f and maximum elastin degradation factor φ_{hm}^e . In our computational results, we sampled aneurysmal growth for different original homeostatic gain ratios $K_{\tau\sigma,o} \in [0, 1]$ as it proved crucial for the G&R vs. FSGe comparison. The circumferential, axial, and temporal factors are

$$f(\theta, z, t) = f_\theta f_z f_t, \quad f_\theta = \exp\left(-\left|\frac{\theta_o - \pi}{\theta_{od}}\right|^{v_\theta}\right), \quad f_z = \exp\left(-\left|\frac{z_o}{z_{od}} - \frac{1}{2}\right|^{v_z}\right), \quad f_t = \frac{\tanh(2t/t_{max})}{\tanh(2)}, \quad t > 0, \quad (37)$$

where the insult is ramped up over the load steps t_{\max} . Recall that load step $t = 0$ corresponds to the CMMe pre-loading stage, whereas $t > 0$ corresponds to G&R. We modulate the temporal factor f_t with the hyperbolic tangent to yield approximately equal displacement increments in all load steps; this enables using a linear predictor that initializes each load step with a solution close to the converged one. The spatial insult profile $f_\theta f_z$ is visualized in Figure 3 (left). We introduce an aneurysmal region locally at the top of the blood vessel, whereas the ends and the bottom maintain healthy parameters.

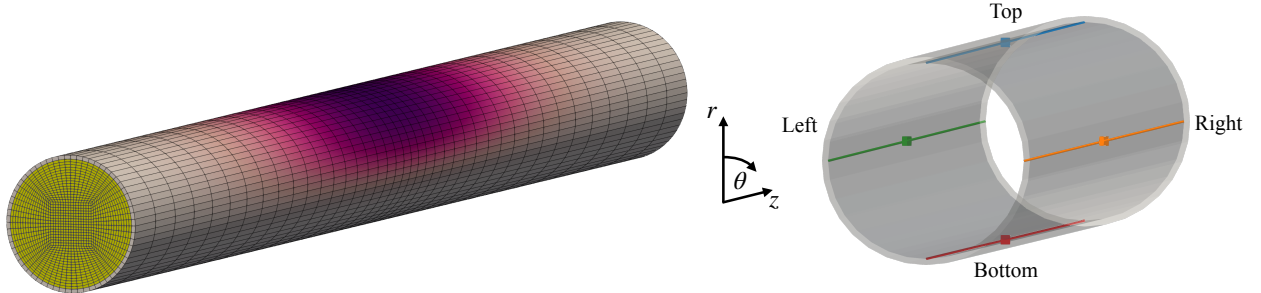


Figure 3: Mesh (left) with fluid domain \mathcal{F} (yellow) and solid domain \mathcal{S} , colored by the spatial insult profile $f_\theta f_z$ (white healthy, purple initiating insult profile). Plot locations (right), top, right, bottom, left, with a cylindrical coordinate system (r, θ, z) .

We generated the cylindrical structured mesh in Figure 3 (left) with hexahedral linear displacement-based finite elements that are refined at the location of the aneurysm in the middle. Further, the mesh has a conforming interface between fluid and solid domains. The global (θ, r, z) coordinate system and four different plot locations within the blood vessel are shown in Figure 3 (right). All results in this work are extracted at the fluid-solid interface, i.e., at the endothelium. We show plots over the axial length of the vessel and point-wise results at the apex of the aneurysm.

4.1. Computational performance

Figure 4 shows the cumulative number of FSGe coupling iterations in each load step for varying gain ratios $K_{\tau\sigma} \in [0, 1]$ required to reach the coupling tolerance ϵ_0 . Load step $t = 0$ denotes the CMMe pre-loading step, which takes only three iterations to converge in all simulations since the displacements \mathbf{d} are close to zero during pre-loading. Our IQN-ILS coupling scheme from Algorithm 6 relies on solutions from previous coupling iterations, which are not yet available at the beginning of load step $t = 1$. In addition, since there is only one prior converged load step, we cannot use extrapolation for the predictor. Thus, load step $t = 1$ requires more coupling iterations than other load steps in all simulations. Importantly, there is a clear trend that more coupling iterations are required with higher $K_{\tau\sigma,o}$. The average number of coupling iterations for load steps 2 to 10 ranges from 2.0 for $K_{\tau\sigma,o} = 0.0$ to 7.6 for $K_{\tau\sigma,o} = 1.0$. For the longest simulation $K_{\tau\sigma,o} = 1.0$ with 84 coupling iterations, the total wall times on an Apple M2 Max CPU were 2.7 min (one core) for linear-elastic mesh deformation and 52 min (six cores) for fluid dynamics in the fluid domain \mathcal{F} and 1.7 min (one core) for G&R with CMMe in the solid domain \mathcal{S} . This renders the steady-state fluid simulation the computational bottleneck of FSGe.

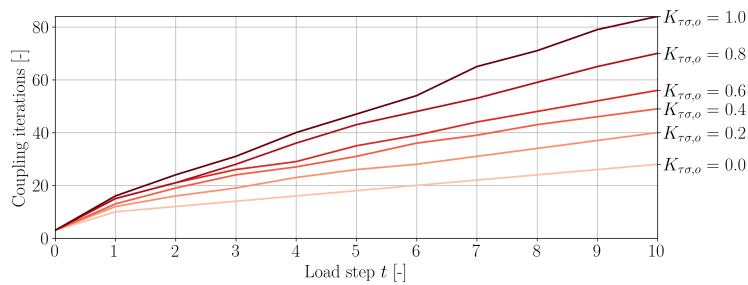


Figure 4: Cumulative number of FSGe coupling iterations per load step for different gain ratios $K_{\tau\sigma,o}$.

4.2. Solid mechanics

This section compares the solid mechanics between solid-only G&R simulations and coupled FSGe simulations, both using CMME as the solid model. Figure 5 shows the displacement fields for G&R (left column) and FSGe (right column) for increasing original homeostatic gain ratios $K_{\tau\sigma,o} \in [0, 1]$ from top to bottom. The red color corresponds to the evolved gain ratio $K_{\tau\sigma,h}$ after applying the aneurysm insult. Note that the evolved blood vessel retains its healthy original homeostatic parameters outside the top part of the aneurysm where the aneurysm insult was applied. Generally, a smaller original homeostatic gain ratio $K_{\tau\sigma,o}$ leads to larger aneurysm growth. Comparing the top row with uniform $K_{\tau\sigma,o} = 0.0$, there is little difference between G&R and FSGe results. However, the aneurysms are smaller with FSGe than with G&R for $K_{\tau\sigma,o} > 0$. The differences become more pronounced for increasing gain ratio $K_{\tau\sigma,o} \rightarrow 1.0$, especially in the bottom aneurysmal region with intact elastin stiffness and mechanosensation. Interestingly, the radial deformation in this region is close to zero for $K_{\tau\sigma,o} = 0.2$ and becomes negative, i.e., inward, for $K_{\tau\sigma,o} > 0.2$.

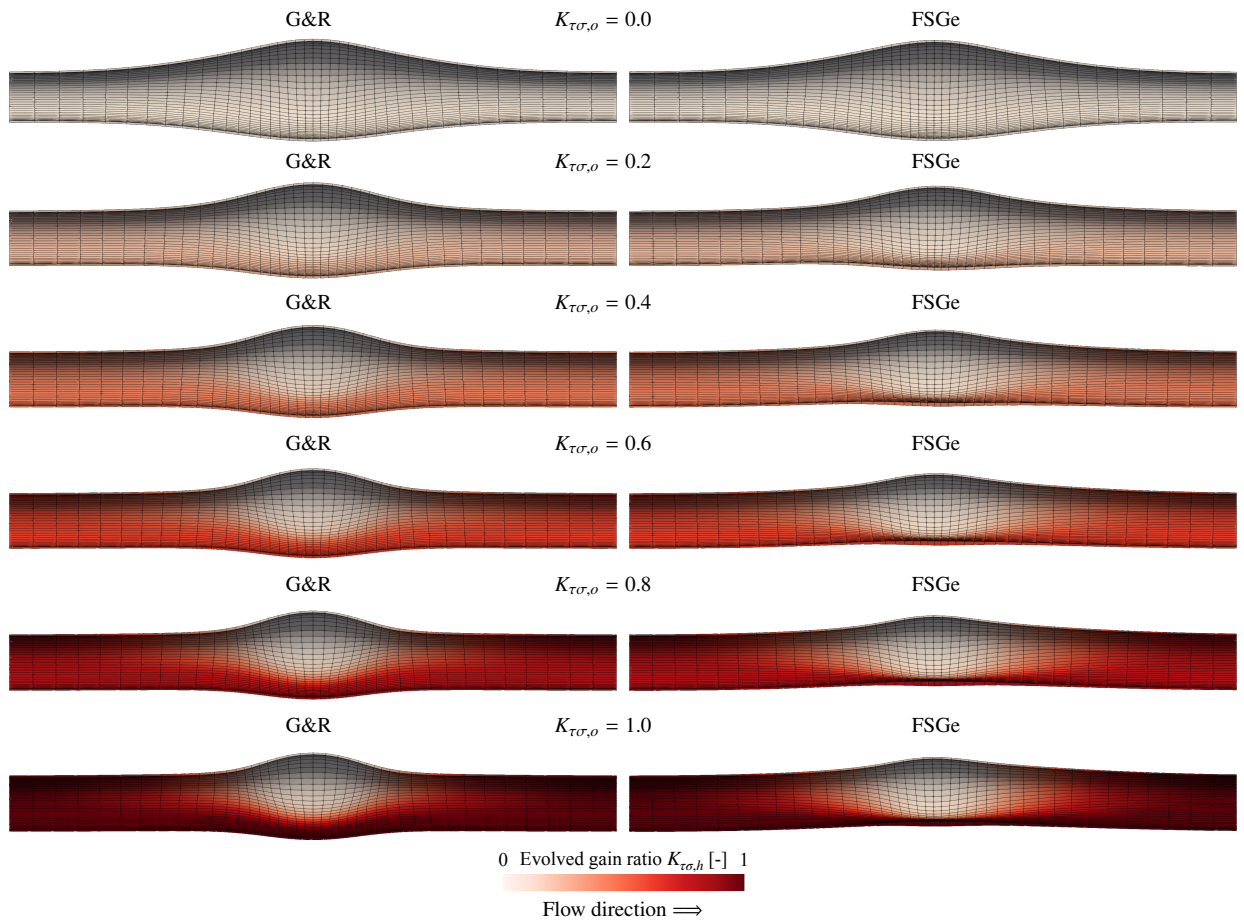


Figure 5: Long-term evolved solid domains in G&R (left) vs. FSGe (right) for different original gain ratios $K_{\tau\sigma,o} \in [0, 1]$ (from top to bottom). The geometries are colored by the evolved gain ratio $K_{\tau\sigma,h}$.

Figure 6 shows the local thickness over the axial length, z , of the blood vessel for $K_{\tau\sigma,o} \in \{0.0, 1.0\}$, i.e., for the top and bottom rows in Figure 5. Again, G&R and FSGe models were very similar for $K_{\tau\sigma,o} = 0.0$ (top row). While all G&R results are symmetric, we observed minor thickening of about 3% downstream at $z = 11$ compared to upstream at $z = 4$ for the FSGe model. With $K_{\tau\sigma,o} = 1.0$, there was a pronounced axial asymmetry in the FSGe model (bottom right) compared to the G&R model (bottom left). Comparing the same locations, we observed 12% downstream thinning at the top of the aneurysm (blue) and 24% thickening at the bottom (red). Most importantly, the

thickness at the bottom of the aneurysm (red) reaches an evolved equilibrated thickness of more than three times the original homeostatic value.

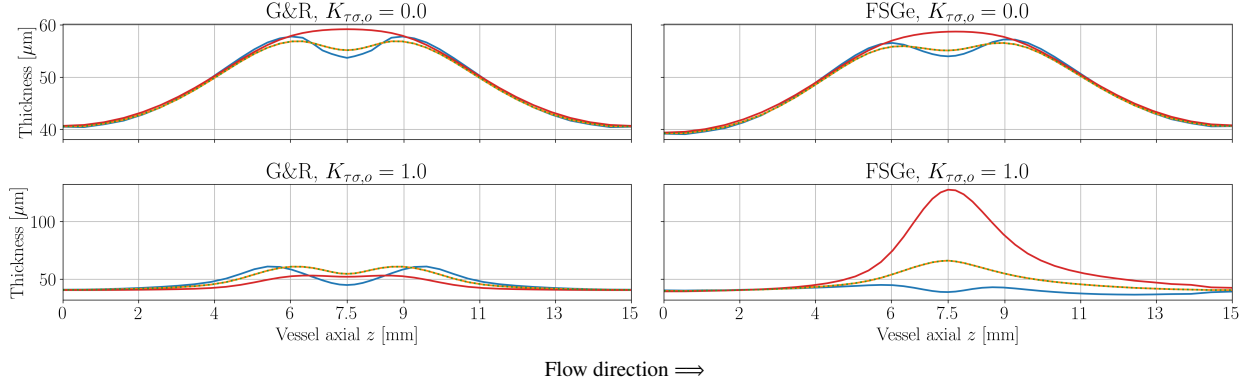


Figure 6: Thickness according to locations in Fig. 3: top (blue), bottom (red), sides (orange/green).

The local displacements $d_{\{\theta,r,z\}}$ in the cylindrical coordinate system are shown in Figure 7. The comparison is shown for the highest sampled gain ratio $K_{\tau\sigma,o} = 1.0$ (bottom row of Figure 5), which showed the most pronounced differences between the two models. Due to the symmetry of the aneurysm, there were no circumferential displacements (top row) at the top and bottom (blue/red dotted) of the aneurysm in both models. However, at the sides of the aneurysm (orange, green), there was double the circumferential displacement, i.e. rotation, towards the bottom with FSGe than with G&R. The radial displacements (middle row) at the bottom (red) and the sides (orange/green dotted) of the aneurysm became negative in the FSGe model, indicating inward growth in these regions. Given the symmetry of the G&R model, axial displacements (bottom row) are symmetric around $z = 7.5$ mm but asymmetric in the FSGe model.

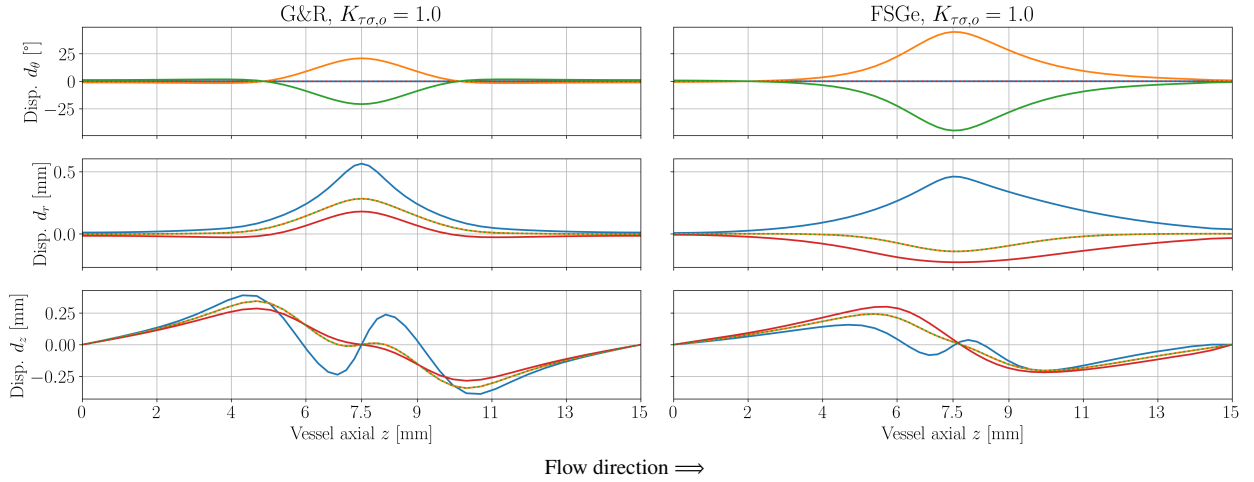


Figure 7: Displacements d_{θ}, d_r, d_z (top to bottom) at the endothelium according to locations in Fig. 3: top (blue), right (orange), bottom (red), left (green) for varying original homeostatic gain ratios $K_{\tau\sigma,o}$.

The local mechanobiology in both G&R and FSGe for $K_{\tau\sigma,o} = 1.0$ is visualized in Figure 8. The prescribed insult profile (top row) of mechanosensation loss towards the top of the aneurysm is identical in both models. However, the same prescribed gain ratios $K_{\tau\sigma,h} = \Delta\sigma_I/\Delta\tau_w$ are achieved with different levels of intramural stimuli $\Delta\sigma_I$ (middle row) and wall shear stress (WSS) stimuli $\Delta\tau_w$ (bottom row). Since $K_{\tau\sigma,h} = 0$ at the top peak of the aneurysm (blue curves at $z = 7.5$), it follows for both models that $\Delta\sigma_I = 0$ at this location. Furthermore, recall that we maintain intact mechanosensation at the bottom of the aneurysm (red curves at $z = 7.5$). While in the G&R model, the

mechanobiologically equilibrated solution yields $K_{\tau\sigma,h} = 1.0 \approx (-0.1)/(-0.1)$, the FSGe model yields $K_{\tau\sigma,h} = 1.0 \approx (-0.45)/(-0.45)$. This means that in the G&R model's evolved equilibrium, both intramural stimulus $\Delta\sigma_I$ and WSS stimulus $\Delta\tau_w$ are reduced by 10% compared to the original homeostatic state. However, in the FSGe model, these were reduced by 45%, thus arriving at a significantly different long-term evolved equilibrium that's characterized by the observed differences in local thickness (Figure 6) and displacements (Figure 7).

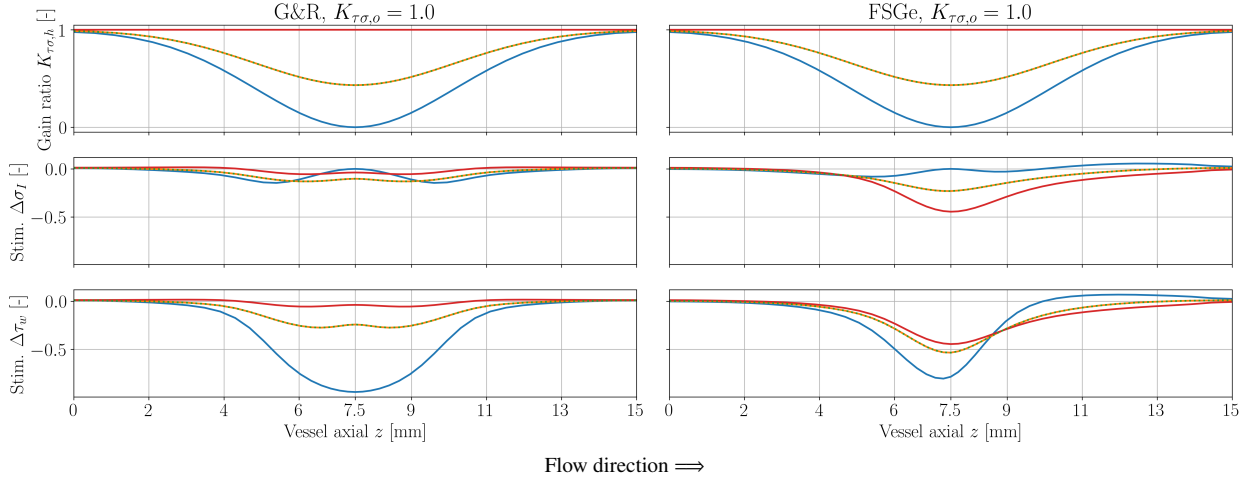


Figure 8: Prescribed evolved equilibrium gain ratio $K_{\tau\sigma,h} = \Delta\sigma_I/\Delta\tau_w$ (top) and resulting intramural $\Delta\sigma_I$ (middle) and WSS stimuli $\Delta\tau_w$ (bottom) in G&R (left) and FSGe (right) models. Locations according to Figure 3: top (blue), bottom (red), sides (orange/green).

We visualize the evolved local collagen mass $\phi_h^c J_h$ in Figure 9 at the aneurysm mid-section over the sampled original gain ratios $K_{\tau\sigma,o}$. Overall, collagen is deposited most at the top of the aneurysm (blue) and, to a lesser extent, at the healthy bottom (red). Notably, with increasing gain ratio $K_{\tau\sigma,o} \rightarrow 1$ in the FSGe model (right), collagen is degraded at the bottom (red) below its initial mass fraction of $\phi_o^c = 0.33$ (black). The degradation of collagen at the bottom (red) of the aneurysm is associated with inward growth around this region. This is visible in Figure 10, where radial displacements at the sides (green/orange) and bottom (red) become negative for $K_{\tau\sigma} \geq 0.4$. These mechanisms are much less evident in the G&R model, where there is little dependence on the original gain ratio $K_{\tau\sigma,o}$ and no collagen degradation.

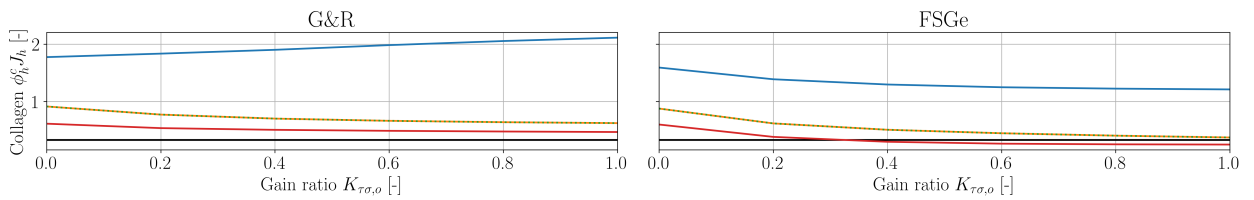


Figure 9: Evolved referential collagen mass fraction (mass of collagen per unit reference volume) $\phi_h^c J_h$ at the endothelium at $z = 7.5$ mm for varying original gain ratios $K_{\tau\sigma,o}$. The black line indicates the reference collagen mass of $\phi_o^c = 0.33$. Locations according to Fig. 3: top (blue), bottom (red), sides (orange/green).

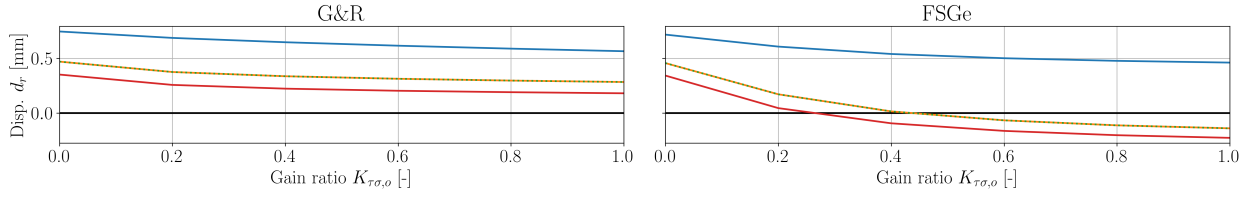


Figure 10: Radial displacement d_r at the endothelium at $z = 7.5$ mm for varying original gain ratios $K_{\tau\sigma,o}$. Displacements $d_r < 0$ (black line) indicate an inward growth of the aneurysm. Locations according to Fig. 3: top (blue), bottom (red), sides (orange/green).

4.3. Fluid dynamics

We compared solid mechanics in G&R and FSGe models in Section 4.2. This section compares the fluid dynamics in both models. Figure 11 shows the WSS stimulus $\Delta\tau_w$ for G&R (left column) and FSGe (right column) simulations. The plot locations are identical to Figure 5. Whereas the WSS stimulus in the FSGe model stems from solving the incompressible Navier-Stokes equations (3), it is approximated from the Poiseuille solution (1) in the G&R model. Purple regions with a value of $\Delta\tau_w \approx 0$ correspond to regions that maintain WSS during the development of the aneurysm. As expected, a higher gain ratio $K_{\tau\sigma,o} \rightarrow 1$ (from top to bottom) leads to more regions with $\Delta\tau_w \rightarrow 0$ due to the increasing weight of WSS in finding the mechanobiological equilibrium. In G&R, $\Delta\tau_w$ is strictly coupled to the vessel's local change in endothelial radius, leading to strong circumferential variations in the apex of the aneurysm. In FSGe, $\Delta\tau_w$ is circumferentially more uniform around the deformed centerline of the blood vessel.

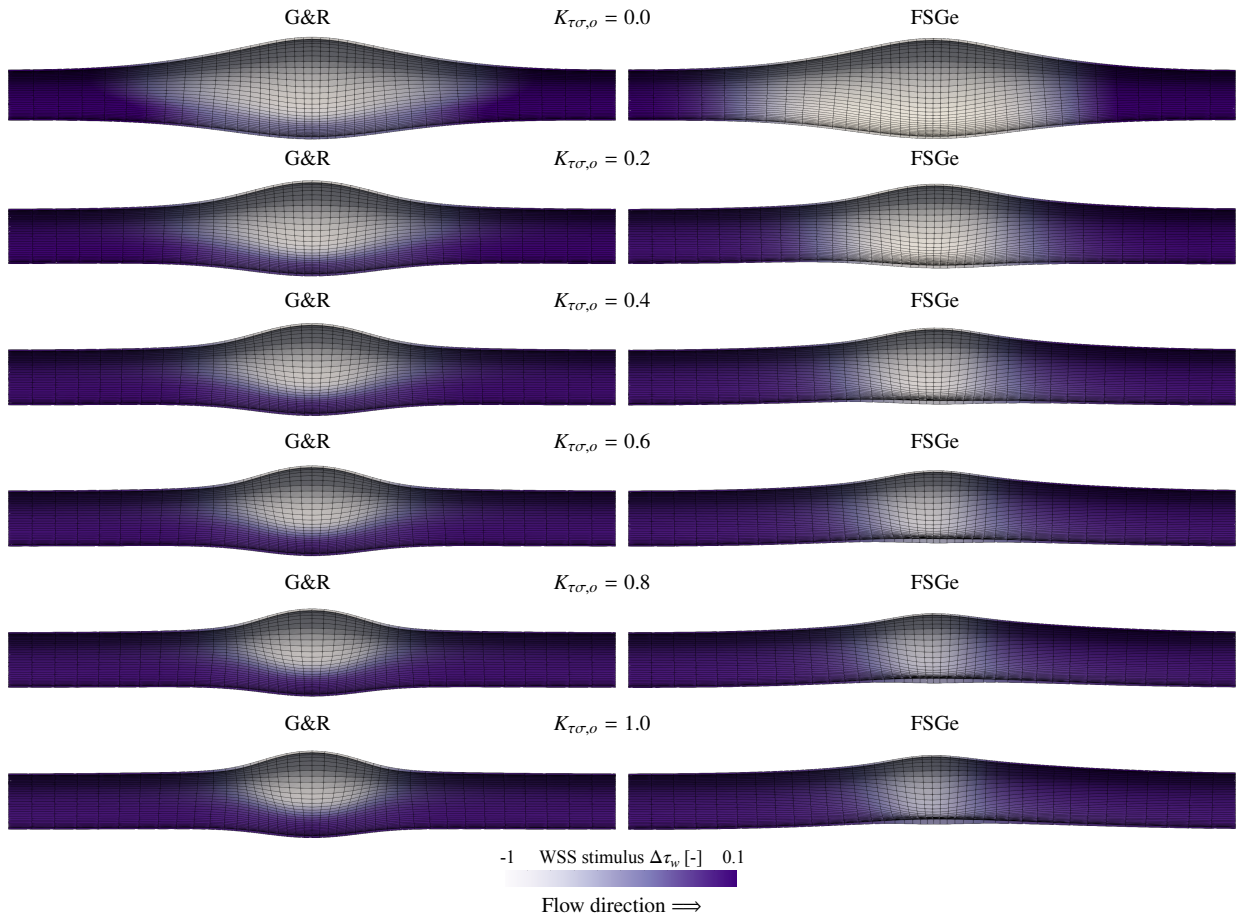


Figure 11: WSS stimulus $\Delta\tau_w$ in G&R (left) vs. FSGe (right) for different original gain ratios $K_{\tau\sigma,o} \in [0, 1]$ (from top to bottom).

Figure 12 shows velocity (left) and pressure (right) for the vessel's longitudinal midsection for different gain ratios $K_{\tau\sigma,o}$ in the FSGe. Note that, due to the absence of local fluid dynamics in the G&R model, we cannot compare the models. The geometries correspond to the right column in Figure 5. Recalling the fluid boundary conditions from Section 4, it is evident that all flows have identical (parabolic) inflow conditions on the very left and identical outflow pressures of 104.9 mmHg on the very right. While there is little variation in pressure fields for the sampled gain ratios $K_{\tau\sigma,o}$, there are some notable differences in the velocity field. There is a small recirculation zone visible at the top apex of the aneurysm. Due to the incompressibility of blood, for $K_{\tau\sigma,o} = 0.0$ (top), the doubling in radius inside the aneurysm drastically decreases local velocity. This effect is less pronounced as the maximum radius decreases with increasing gain ratio $K_{\tau\sigma,o}$. Interestingly, as the gain ratio approaches $K_{\tau\sigma,o} \rightarrow 1$, the velocity is deflected upward into the top part upstream of the aneurysm.

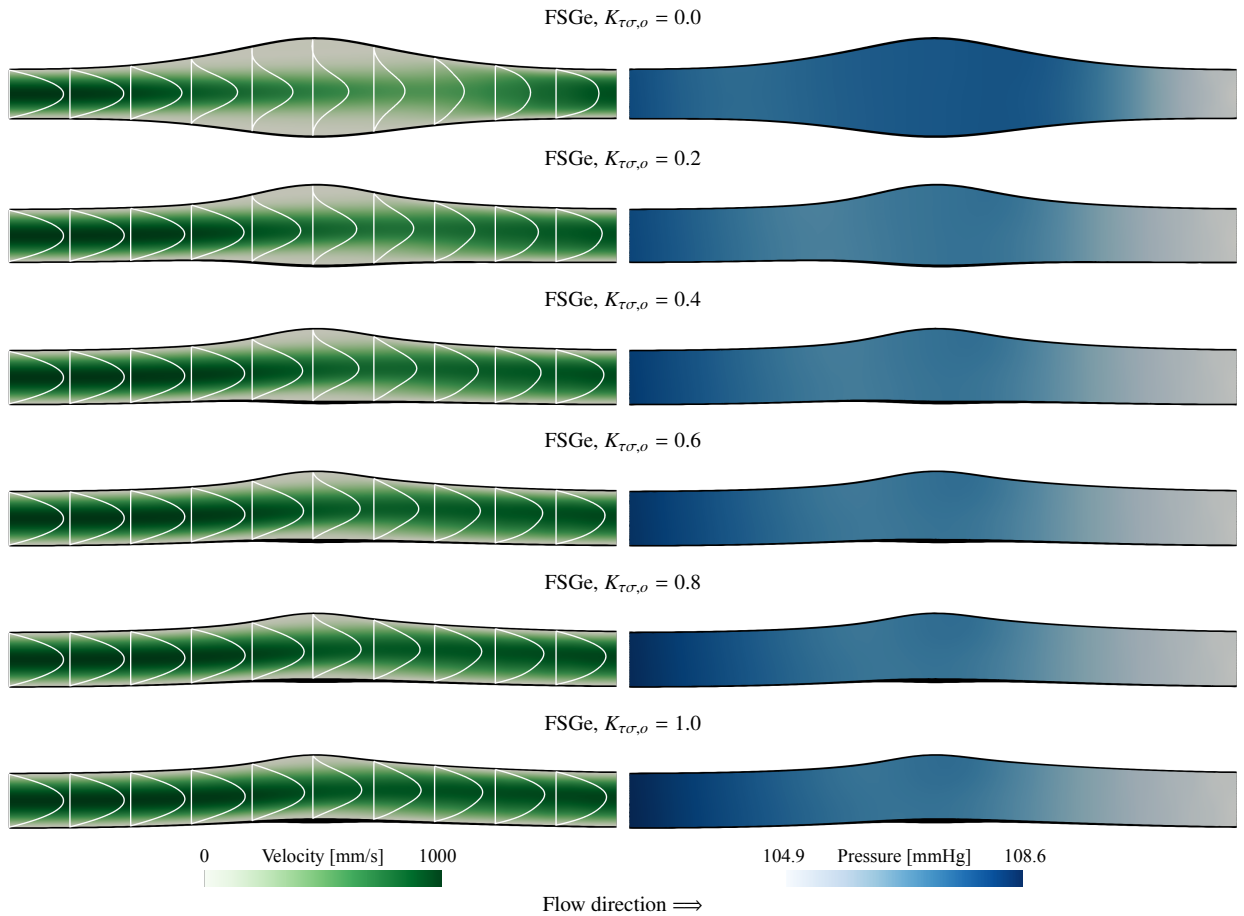


Figure 12: Fluid domains in FSGe models with velocity and flow profiles (left) and pressure (right) with vessel wall (black) for original homeostatic gain ratios $K_{\tau\sigma,o} \in [0, 1]$ (from top to bottom).

Figure 13 shows fluid velocity \mathbf{u} (left) and pressure p (right) along the deformed centerline of the vessel for all gain ratios in Figure 12. Again, prescribed boundary conditions are evident for the inlet velocity at $z = 0$ mm and outlet pressure at $z = 15$ mm. The centerline velocity also coincides with the region of maximum velocity. The drop in velocity inside the aneurysm and the downstream acceleration distal to the aneurysm are visible. We also observe a linear drop in pressure along z upstream and downstream of the aneurysm and a pressure plateau in the aneurysmal region. While there's a more than 60% fluctuation in centerline velocity throughout all $K_{\tau\sigma,o}$ samples, the pressure changes only about 3.5% compared to the overall mean pressure.

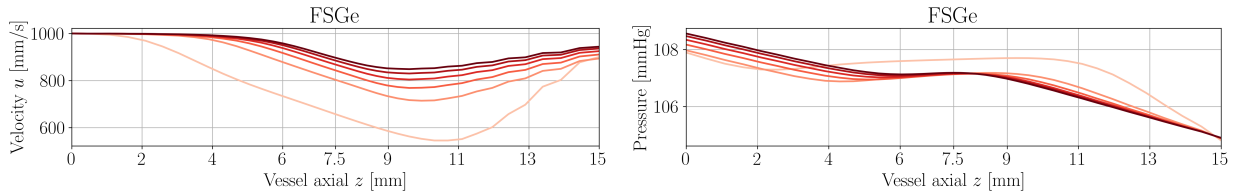


Figure 13: Velocity magnitude (left) and pressure (right) along the deformed vessel centerline from $K_{\tau\sigma,o} = 0.0$ (light) to $K_{\tau\sigma,o} = 1.0$ (dark).

5. Discussion

We presented a novel equilibrated fluid-solid-growth (FSGe) method, where we strongly couple the three-dimensional (3D) Navier-Stokes equations and the 3D equilibrated constrained mixture model (CMMe). We demonstrated crucial differences in the solution compared to a solid-only growth and remodeling (G&R) model in illustrative computational examples of an asymmetric aortic aneurysm. We identified the original homeostatic gain ratio $K_{\tau\sigma,o}$ as a crucial factor determining the degree of interaction between fluid and solid growth in the long-term evolution. In the remainder of this section, we discuss the results from Section 4, limitations, and future perspectives. We first review computational aspects of the FSGe method proposed in this work: its equilibrated nature (5.1), its strong coupling (5.2), stability of CMMe (5.3), and original homeostasis (5.4). We further review mechanobiological aspects of FSGe, namely wall shear stress (WSS) influence (5.5) and the directionality and pulsatility of blood flow (5.6).

5.1. Equilibrated vs. transient growth and remodeling

Latorre and Humphrey [5] introduced the CMMe as a fast, rate-independent version of the constrained mixture model (CMM). It directly yields the long-term equilibrated G&R response, i.e., at $s \rightarrow \infty$. The computational cost of CMMe is comparable to a solid mechanics FEM solution with a hyperelastic material. Together with our implicit coupling scheme, this makes the FSGe highly efficient. On the other hand, it may be critical to model transient G&R in cases where the insult is applied slowly compared to the G&R response. For example, tissue-engineered vascular grafts (TEVGs) in Fontan patients can develop a severe stenosis, which sometimes spontaneously resolves [14, 15]. Here, the time-resolved development of G&R is crucial to studying the mechanisms behind the stenosis formation and resolution [13], which can be modeled with FSGe [12]. However, we can only study phenomena that will yield a long-term mechanobiological equilibrium. Yet, many clinically interesting applications involve G&R processes that do not necessarily yield an evolved equilibrium state [57]. For example, theories have been developed to quantify the stability or instability of G&R processes such as aneurysm formation [58, 59]. Thus, transient G&R models like the one developed by Schwarz et al. [13] will be necessary to study fluid-solid-growth interaction (FSG) in unstable cases.

5.2. Strong vs. weak fluid-solid-growth coupling

We proposed a strongly coupled partitioned fluid-structure interaction model where the solid G&R model is given by the CMMe. A fully implicit monolithic coupling scheme is intractable in this case due to the discrepancy in time scales, $T_f \sim 1$ ms for the fluid and $T_s \rightarrow \infty$ for the solid CMMe. Our coupling algorithm converged in only two coupling iterations for $K_{\tau\sigma,o} = 0.0$, allowing for a weakly coupled partitioned scheme. However, the number of coupling iterations rose with $K_{\tau\sigma,o} \rightarrow 1$, highlighting the strong interaction between fluid and solid. We experimented with static relaxation for FSGe coupling. However, this required a very low relaxation parameter ω to stabilize the coupling scheme, which led to excessive coupling iterations. We achieved considerable speedups by introducing dynamic Aitken relaxation [50] but could not find a solution for high $K_{\tau\sigma,o} \rightarrow 1$. Thus, IQN-ILS remains our coupling algorithm of choice [45]. More speedup could be achieved by taking into account the iterations internal to each solver [60].

5.3. Computational stability of the equilibrated constrained mixture model

In addition to potential instabilities arising from the fluid-structure coupling in FSGe (Section 5.2), we discovered instabilities in the underlying solid CMMe model for $K_{\tau\sigma,o} \rightarrow 1$, leading to oscillations in displacements, Jacobian,

and internal G&R variables. These are triggered by the growth of the aneurysm and can be interpreted as a mechanical instability problem. There may exist other biological equilibria of $\Delta\tau_w$ and $\Delta\sigma_I$ that satisfy a certain gain ratio $K_{\tau\sigma,o} > 0$. Only the special case $K_{\tau\sigma,o} = 0 = \Delta\sigma_I$ has a unique biological solution for $\Delta\sigma_I$. A mechanobiologically equilibrated solution is obtained by simultaneously solving for a mechanical equilibrium (4). We believe these oscillations originate from evaluating the mechanobiological equilibrium (12) point-wise on each Gauß-point, without having any continuity conditions for internal G&R variables. Thus, it is possible that Gauß-points within the same element may converge to different mechanobiological equilibria. We currently prevent these oscillations by choosing only one element across the vessel thickness. A more versatile solution could be using an internal G&R variable, e.g., collagen mass fraction ϕ_h^c , as an additional unknown in addition to the displacements and choosing a lower polynomial order for its shape function. Element formulations could be adopted from (quasi)-incompressibility formulations, e.g., mixed-field approaches such as Q1P0 [61] or MINI elements [62]. Alternatively, a functional could be added to the solid weak form preventing oscillations in collagen mass fraction. This idea is derived from edge stabilization in computational fluid dynamics (CFD), where a least-squares term penalizes the jump in the gradient of the discrete solution over element boundaries [63].

5.4. Definition of original homeostasis

In computational biomechanics, the solid reference configuration, often obtained from *in vivo* medical imaging, is typically not stress-free due to fluid or other loads. This requires either finding a stress-free reference configuration, which might not exist [64], or local residual stresses so that the initial configuration is in equilibrium with fluid loads. Many strategies have been developed to address this issue [65–67]. In G&R, we need to satisfy a *biological* equilibrium, i.e., original homeostasis o , in addition to the aforementioned *mechanical* equilibrium. In this work, we achieve a mechanobiological equilibrated original homeostasis by solving a non-linear equation for a thin-walled cylinder for the initial *in vivo* blood pressure P_o . Here, the inner and outer radii are fixed, as well as the homeostatic parameters in Table 2. This approach works well in a given ideal cylinder with an unknown uniform *in vivo* blood pressure that can be freely chosen in the model. However, it cannot be generalized to *in vivo* blood vessel geometries that were imaged under measured blood pressure. Given the limited prior work with 3D CMM, there are few references for pre-loading *in vivo* G&R models. The algorithm proposed by Wu et al. [68] solves a minimization problem by locally varying fiber alignment. Laubrie et al. [69] prescribed a transmurally varying prestretch gradient for constituents to establish an initial homeostatic state. Gebauer et al. [70] introduced an iterative algorithm to prestress a fixed patient-specific cardiac geometry under fixed ventricular pressures. The algorithm solves for the local isotropic elastin prestretch until the model is in mechanobiological equilibrium up to a specified displacement tolerance. The choice of elastin prestretch was motivated by the fact that elastin is the only constituent that is assumed to not turn over in the G&R time scale considered, given its long half-life [71]. In the future, this approach could be used to define the original homeostasis in FSGe problems by either locally solving for the elastin prestretch or other quantities, such as vessel thickness.

5.5. Influence of local wall shear stress

Previous FSG studies did not investigate differences across G&R models or found only minor differences [13]. We observed in Section 4.2 that both G&R and FSGe models delivered similar results for $K_{\tau\sigma,o} \rightarrow 0$ despite the underlying assumptions in the purely solid G&R model. However, for high gain ratios $K_{\tau\sigma,o} \rightarrow 1$, the different long-term evolved equilibria between G&R and FSGe models became more pronounced. These differences were especially prevalent in the bottom healthy region of the blood vessel with intact elastin stiffness and mechanosensation. Compared to G&R, the FSGe model grew *inward* with a three-fold *increase* in vessel wall thickness. Furthermore, in Section 4.3, we observed that the inward growth of the bottom region of the blood vessel is associated with an upward deflection of blood flow toward the top of the aneurysm.

As mentioned previously, earlier versions of G&R relied on the Poiseuille and thin-walled cylinder assumptions to calculate mechanical stimuli. Assuming Poiseuille flow (1) and a thin-walled cylinder for the blood vessel, analytic relationships can be derived for WSS τ_w and wall stress σ components, respectively,

$$\tau_w \sim Q \cdot \frac{1}{r^3}, \quad \sigma_\theta \sim P \cdot \frac{r}{h}, \quad \sigma_r \sim -P, \quad \sigma_z \sim F \cdot \frac{1}{rh}, \quad (38)$$

with radius r , wall thickness h , flow rate Q , pressure P , and axial force F . We specifically developed our FSGe coupling method to *not* rely on Poiseuille flow and thin-walled assumptions but rather the numerical solution of the 3D Navier-Stokes equations and 3D finite strain elasticity, respectively. Yet, we studied aneurysmal development under steady-state flow with a low Reynolds number of $Re \approx 170$ which resulted in a flow profile similar to parabolic even in aneurysmal regions of the blood vessel. Thus, comparing the fluid and solid field solutions derived from our FSGe model to these simplifying assumptions gives us insights into the feedback loop of biomechanically regulated variables (Figure 1) and helps us explain the differences in mechanobiological equilibria. In our examples, the flow rate Q was constant, and there was little change in local pressure P throughout the fluid domain. We can thus derive the following relationships for the change in WSS and intramural stimuli

$$\Delta\tau_w \sim \frac{r_o^3}{r_h^3} - 1, \quad (39)$$

$$\Delta\sigma_I \sim \frac{h_o}{r_o} \frac{r_h}{h_h} - 1. \quad (40)$$

The differences in aneurysmal growth were associated with these different definitions of stimuli and, therefore, different values of mechanobiological equilibria in the two models. Our illustrative computational examples highlight the importance of incorporating local fluid-derived WSS in the FSGe model. In the FSGe model, the fluid couples the deformation in the aneurysmal top part of the blood vessel with the healthy bottom part. In the purely solid G&R model, the WSS in these regions is evaluated independently from local deformations. The stimuli $\Delta\tau_w < 0$ and $\Delta\sigma_I < 0$ were downregulated to a much larger extent in FSGe than in G&R at the bottom of the aneurysm. In the G&R model, relying on relationship (39) resulted in an increase in evolved radius r_h and thickness h_h . In the FSGe model, the fluid-derived WSS, $\Delta\tau_w$ decreased with decreasing r_h which is contrary to (39). This was possible due to the Navier-Stokes-derived WSS (Figure 11, right) and the upward deflection of the blood flow inside the aneurysm (Figure 12). In both models, this change was accompanied by an increase in thickness h_h according to (40).

5.6. Pulsatility and directionality of blood flow

Our FSGe model considered steady-state flow conditions as an input for the intramural and WSS G&R stimuli, $\Delta\sigma_I$ and $\Delta\tau_w$, respectively. This is equivalent to some previous FSG methods in Table 1, whereas others used time-averaged G&R stimuli from a pulsatile flow simulation. Pulsatility is an important determinant of the blood vessel wall geometry, structure, and properties [72, 73]. For example, Eberth et al. [74] found that increased wall thickness in hypertension correlated more strongly with pulse than with mean or systolic pressure. Extending our FSGe approach to incorporate pulsatility would require solving an fluid-structure interaction (FSI) problem with an elastic wall in each coupling iteration. We could then extract the instantaneous elastic properties of the CMME with a fixed G&R state from the evolved equilibrium state, as shown by Latorre and Humphrey [5]. In the aneurysmal region, we currently introduce dysfunctional mechanosensing at the endothelium by regionally setting $K_{\tau\sigma,o} \rightarrow 0$ in the top part of the aneurysm [56] as a model input. In the future, mechanosensing could be a function of pulsatility and thus as part of the model prediction.

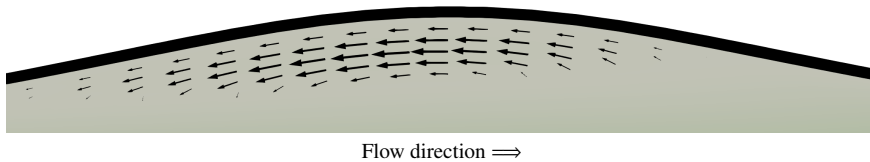


Figure 14: Recirculation zone in an FSGe simulation with $K_{\tau\sigma,o} = 0.0$ (top left in Figure 12), with backflow velocity vectors for $u_z < 0$ at the top of the aneurysm.

Another crucial input would be the variability of WSS over a cardiac cycle. Figure 14 shows a recirculation zone with backflow against the predominant flow direction at the top of the aneurysm. This flow separation only occurs in the FSGe model with $K_{\tau\sigma,o} = 0.0$ (top left in Figure 12) due to its nearly two-fold increase in radius. Note, however, that the maximum backflow velocity is only 1.6% of the maximum inlet velocity. This effectively reverses the direction

of the local WSS vector τ_w acting on the vessel wall. However, in solid G&R models, τ_w can only be estimated as a scalar quantity to inform the WSS stimulus, typically derived from Poiseuille flow (1). It is well established that not only the magnitude but also the pulsatility and direction of WSS are constantly sensed by the endothelium [75, 76]. For example, the directionality of WSS plays an important role in the development of atherosclerosis [77]. Mohamied et al. [78] proposed a new metric,

$$\text{transWSS} = \frac{1}{T} \int_0^T \frac{\tau_w \cdot (\mathbf{n} \times \tau_{\text{mean}})}{\|\tau_{\text{mean}}\|} dt, \quad \tau_{\text{mean}} = \frac{1}{T} \int_0^T \tau_w dt, \quad (41)$$

to quantify the change of direction of WSS over the course of a cardiac cycle T , with vessel normal vector \mathbf{n} and mean WSS vector τ_{mean} . This metric was shown to correlate better with atherosclerotic lesion prevalence than other metrics like time-averaged or oscillatory WSS index. Our FSGe approach allows locally quantifying directionality measures like transWSS. In the future, incorporating local and directional WSS will enable the testing of hypotheses in FSGe-mediated aneurysm growth and atherosclerotic lesion formation using FSGe. Since current G&R models were designed with the static and scalar nature of reduced fluid dynamics in mind, we expect future biological insights from FSGe to arise from the advancements outlined in this work.

6. Acknowledgements

This work was supported by NIH Grants K99HL161313, R01HL139796, R01HL159954, the Stanford Maternal and Child Health Research Institute, and the Additional Ventures Foundation Cures Collaborative. We further thank Dr. Richard Schussnig for his help with IQN-ILS and Drs. Alice Cortinovis and Luca Pegolotti for their help with linear solvers. In addition, we thank Drs. Yuri Bazilevs, Fabian Bräu, David Li, Matteo Salvador, and Vijay Vedula for stimulating discussions on the stability of the CMMe model.

References

- [1] S. Loerakker, J. D. Humphrey, Computer model-driven design in cardiovascular regenerative medicine, *Annals of Biomedical Engineering* 51 (1) (2022) 45–57. doi:10.1007/s10439-022-03037-5.
- [2] J. D. Humphrey, K. R. Rajagopal, A constrained mixture model for growth and remodeling of soft tissues, *Mathematical Models and Methods in Applied Sciences* 12 (03) (2002) 407–430. doi:10.1142/s0218202502001714.
- [3] J. D. Humphrey, Constrained mixture models of soft tissue growth and remodeling – twenty years after, *Journal of Elasticity* 145 (1-2) (2021) 49–75. doi:10.1007/s10659-020-09809-1.
- [4] D. Dajnowiec, B. Langille, Arterial adaptations to chronic changes in haemodynamic function: coupling vasomotor tone to structural remodeling, *Clinical Science* 113 (1) (2007) 15–23. doi:10.1042/cs20060337.
- [5] M. Latorre, J. D. Humphrey, Fast, rate-independent, finite element implementation of a 3d constrained mixture model of soft tissue growth and remodeling, *Computer Methods in Applied Mechanics and Engineering* 368 (2020) 113156. doi:10.1016/j.cma.2020.113156.
- [6] T. W. Secomb, *Hemodynamics* (mar 2016). doi:10.1002/cphy.c150038.
- [7] E. L. Schwarz, L. Pegolotti, M. R. Pfaller, A. L. Marsden, Beyond cfd: Emerging methodologies for predictive simulation in cardiovascular health and disease, *Biophysics Reviews* 4 (1) (2023) 011301. arXiv:https://doi.org/10.1063/5.0109400, doi:10.1063/5.0109400.
URL <https://doi.org/10.1063/5.0109400>
- [8] C. A. Figueroa, S. Baek, C. A. Taylor, J. D. Humphrey, A computational framework for fluid–solid-growth modeling in cardiovascular simulations, *Computer Methods in Applied Mechanics and Engineering* 198 (45-46) (2009) 3583–3602. doi:10.1016/j.cma.2008.09.013.
- [9] A. Sheidaei, S. Hunley, S. Zeinali-Davarani, L. Raguin, S. Baek, Simulation of abdominal aortic aneurysm growth with updating hemodynamic loads using a realistic geometry, *Medical Engineering & Physics* 33 (1) (2011) 80–88. doi:10.1016/j.medengphy.2010.09.012.
- [10] P. N. Watton, N. B. Raberger, G. A. Holzapfel, Y. Ventikos, Coupling the hemodynamic environment to the evolution of cerebral aneurysms: Computational framework and numerical examples, *Journal of Biomechanical Engineering* 131 (10) (Sep. 2009). doi:10.1115/1.3192141.
- [11] A. Grytsan, P. N. Watton, G. A. Holzapfel, A thick-walled fluid–solid-growth model of abdominal aortic aneurysm evolution: Application to a patient-specific geometry, *Journal of Biomechanical Engineering* 137 (3) (mar 2015). doi:10.1115/1.4029279.
- [12] M. Latorre, J. M. Szafron, A. B. Ramachandra, J. D. Humphrey, In vivo development of tissue engineered vascular grafts: a fluid-solid-growth model, *Biomechanics and Modeling in Mechanobiology* 21 (3) (2022) 827–848. doi:10.1007/s10237-022-01562-9.
- [13] E. L. Schwarz, M. R. Pfaller, J. M. Szafron, M. Latorre, S. E. Lindsey, C. K. Breuer, J. D. Humphrey, A. L. Marsden, A fluid–solid-growth solver for cardiovascular modeling, *Computer Methods in Applied Mechanics and Engineering* 417 (2023) 116312. doi:10.1016/j.cma.2023.116312.
- [14] E. L. Schwarz, J. M. Kelly, K. M. Blum, K. N. Hor, A. R. Yates, J. C. Zbinden, A. Verma, S. E. Lindsey, A. B. Ramachandra, J. M. Szafron, J. D. Humphrey, T. Shin’oka, A. L. Marsden, C. K. Breuer, Hemodynamic performance of tissue-engineered vascular grafts in fontan patients, *npj Regenerative Medicine* 6 (1) (jul 2021). doi:10.1038/s41536-021-00148-w.
- [15] K. M. Blum, J. C. Zbinden, A. B. Ramachandra, S. E. Lindsey, J. M. Szafron, J. W. Reinhardt, M. Heitkemper, C. A. Best, G. J. M. Mirhaidari, Y.-C. Chang, A. Ulzibayar, J. Kelly, K. V. Shah, J. D. Drews, J. Zakko, S. Miyamoto, Y. Matsuzaki, R. Iwaki, H. Ahmad, R. Daulton, D. Musgrave, M. G. Wiet, E. Heuer, E. Lawson, E. Schwarz, M. R. McDermott, R. Krishnamurthy, R. Krishnamurthy, K. Hor, A. K. Armstrong, B. A. Boe, D. P. Berman, A. J. Trask, J. D. Humphrey, A. L. Marsden, T. Shinoka, C. K. Breuer, Tissue engineered vascular grafts transform into autologous neovessels capable of native function and growth, *Communications Medicine* 2 (1) (jan 2022). doi:10.1038/s43856-021-00063-7.
- [16] A. B. Ramachandra, A. M. Kahn, A. L. Marsden, Patient-specific simulations reveal significant differences in mechanical stimuli in venous and arterial coronary grafts, *Journal of Cardiovascular Translational Research* 9 (4) (2016) 279–290. doi:10.1007/s12265-016-9706-0.
- [17] M. O. Khan, J. S. Tran, H. Zhu, J. Boyd, R. R. S. Packard, R. P. Karlsberg, A. M. Kahn, A. L. Marsden, Low wall shear stress is associated with saphenous vein graft stenosis in patients with coronary artery bypass grafting, *Journal of Cardiovascular Translational Research* 14 (4) (2020) 770–781. doi:10.1007/s12265-020-09982-7.
- [18] I. S. Lan, W. Yang, J. A. Feinstein, J. Kreutzer, R. T. Collins, M. Ma, G. T. Adamson, A. L. Marsden, Virtual transcatheter interventions for peripheral pulmonary artery stenosis in williams and alagille syndromes, *Journal of the American Heart Association* 11 (6) (mar 2022). doi:10.1161/jaha.121.023532.
- [19] J. M. Szafron, W. Yang, J. A. Feinstein, M. Rabinovitch, A. L. Marsden, A computational growth and remodeling framework for adaptive and maladaptive pulmonary arterial hemodynamics, *Biomechanics and Modeling in Mechanobiology* (sep 2023). doi:10.1007/s10237-023-01744-z.
- [20] D. Ambrosi, M. Ben Amar, C. J. Cyron, A. DeSimone, A. Goriely, J. D. Humphrey, E. Kuhl, Growth and remodelling of living tissues: perspectives, challenges and opportunities, *Journal of The Royal Society Interface* 16 (157) (2019) 20190233. doi:10.1098/rsif.2019.0233.
- [21] S. Baek, R. Gleason, K. Rajagopal, J. Humphrey, Theory of small on large: Potential utility in computations of fluid–solid interactions in arteries, *Computer Methods in Applied Mechanics and Engineering* 196 (31-32) (2007) 3070–3078. doi:10.1016/j.cma.2006.06.018.
- [22] C. A. Figueroa, I. E. Vignon-Clementel, K. E. Jansen, T. J. Hughes, C. A. Taylor, A coupled momentum method for modeling blood flow in three-dimensional deformable arteries, *Computer Methods in Applied Mechanics and Engineering* 195 (41-43) (2006) 5685–5706. doi:10.1016/j.cma.2005.11.011.
- [23] M. R. Pfaller, J. Pham, A. Verma, L. Pegolotti, N. M. Wilson, D. W. Parker, W. Yang, A. L. Marsden, Automated generation of 0D and 1D reduced-order models of patient-specific blood flow, *International Journal for Numerical Methods in Biomedical Engineering* 38 (10) (aug 2022). doi:10.1002/cnm.3639.
- [24] svFSIplus (<https://github.com/SimVascular/svFSIplus>) (2024).
URL <https://github.com/SimVascular/svFSIplus>

- [25] C. Zhu, V. Vedula, D. Parker, N. Wilson, S. Shadden, A. Marsden, svFSI: A multiphysics package for integrated cardiac modeling, *Journal of Open Source Software* 7 (78) (2022) 4118. doi:10.21105/joss.04118.
- [26] A. Updegrave, N. M. Wilson, J. Merkow, H. Lan, A. L. Marsden, S. C. Shadden, SimVascular: An open source pipeline for cardiovascular simulation, *Annals of Biomedical Engineering* 45 (3) (2016) 525–541. doi:10.1007/s10439-016-1762-8.
- [27] M. E. Moghadam, I. E. Vignon-Clementel, R. Figliola, A. L. Marsden, A modular numerical method for implicit 0d/3d coupling in cardiovascular finite element simulations, *Journal of Computational Physics* 244 (2013) 63–79. doi:10.1016/j.jcp.2012.07.035.
- [28] M. Esmaily-Moghadam, Y. Bazilevs, A. L. Marsden, A new preconditioning technique for implicitly coupled multidomain simulations with applications to hemodynamics, *Computational Mechanics* 52 (5) (2013) 1141–1152. doi:10.1007/s00466-013-0868-1.
- [29] J. D. Humphrey, S. Na, Elastodynamics and arterial wall stress, *Annals of Biomedical Engineering* 30 (4) (2002) 509–523. doi:10.1114/1.1467676.
- [30] P. Moireau, N. Xiao, M. Astorino, C. A. Figueroa, D. Chapelle, C. A. Taylor, J.-F. Gerbeau, External tissue support and fluid–structure simulation in blood flows, *Biomechanics and Modeling in Mechanobiology* 11 (1–2) (2011) 1–18. doi:10.1007/s10237-011-0289-z.
- [31] A. Valentín, L. Cardamone, S. Baek, J. Humphrey, Complementary vasoactivity and matrix remodelling in arterial adaptations to altered flow and pressure, *Journal of The Royal Society Interface* 6 (32) (2008) 293–306. doi:10.1098/rsif.2008.0254.
- [32] J. S. Wilson, S. Baek, J. D. Humphrey, Importance of initial aortic properties on the evolving regional anisotropy, stiffness and wall thickness of human abdominal aortic aneurysms, *Journal of The Royal Society Interface* 9 (74) (2012) 2047–2058. doi:10.1098/rsif.2012.0097.
- [33] M. Latorre, J. D. Humphrey, Numerical knockouts–in silico assessment of factors predisposing to thoracic aortic aneurysms, *PLOS Computational Biology* 16 (10) (2020) e1008273. doi:10.1371/journal.pcbi.1008273.
- [34] A. B. Ramachandra, M. Latorre, J. M. Szafron, A. L. Marsden, J. D. Humphrey, Vascular adaptation in the presence of external support - a modeling study, *Journal of the Mechanical Behavior of Biomedical Materials* 110 (2020) 103943. doi:10.1016/j.jmbbm.2020.103943.
- [35] J. M. Szafron, R. Khosravi, J. Reinhardt, C. A. Best, M. R. Bersi, T. Yi, C. K. Breuer, J. D. Humphrey, Immuno-driven and mechano-mediated neotissue formation in tissue engineered vascular grafts, *Annals of Biomedical Engineering* 46 (11) (2018) 1938–1950. doi:10.1007/s10439-018-2086-7.
- [36] A. Valentín, J. Humphrey, G. Holzapfel, A finite element-based constrained mixture implementation for arterial growth, remodeling, and adaptation: Theory and numerical verification, *International Journal for Numerical Methods in Biomedical Engineering* 29 (8) (2013) 822–849. doi:10.1002/cnm.2555.
- [37] N. Horvat, L. Virag, G. A. Holzapfel, J. Sorić, I. Karšaj, A finite element implementation of a growth and remodeling model for soft biological tissues: Verification and application to abdominal aortic aneurysms, *Computer Methods in Applied Mechanics and Engineering* 352 (2019) 586–605. doi:10.1016/j.cma.2019.04.041.
- [38] M. Latorre, J. D. Humphrey, A mechanobiologically equilibrated constrained mixture model for growth and remodeling of soft tissues, *ZAMM - Journal of Applied Mathematics and Mechanics / Zeitschrift für Angewandte Mathematik und Mechanik* 98 (12) (2018) 2048–2071. doi:10.1002/zamm.201700302.
- [39] S. A. Maas, B. J. Ellis, G. A. Ateshian, J. A. Weiss, FEBio: Finite elements for biomechanics, *Journal of Biomechanical Engineering* 134 (1) (jan 2012). doi:10.1115/1.4005694.
- [40] S. Goswami, D. S. Li, B. V. Rego, M. Latorre, J. D. Humphrey, G. E. Karniadakis, Neural operator learning of heterogeneous mechanobiological insults contributing to aortic aneurysms, *Journal of The Royal Society Interface* 19 (193) (aug 2022). doi:10.1098/rsif.2022.0410.
- [41] P. R. Amestoy, I. S. Duff, J.-Y. L'Excellent, J. Koster, A fully asynchronous multifrontal solver using distributed dynamic scheduling, *SIAM Journal on Matrix Analysis and Applications* 23 (1) (2001) 15–41. doi:10.1137/s0895479899358194.
- [42] S. Balay, S. Abhyankar, M. Adams, J. Brown, P. Brune, K. Buschelman, L. Dalcin, A. Dener, V. Eijkhout, W. Gropp, et al., *Petsc users manual*, Tech. Rep. No. ANL-95/11 - Revision 2.3.2 (2019).
- [43] J. D. Humphrey, S. L. O'Rourke, *An Introduction to Biomechanics*, Springer New York, 2015. doi:10.1007/978-1-4939-2623-7.
- [44] G. Hou, J. Wang, A. Layton, Numerical methods for fluid–structure interaction — a review, *Communications in Computational Physics* 12 (2) (2012) 337–377. doi:10.4208/cicp.291210.290411s.
- [45] J. Degroote, Partitioned simulation of fluid–structure interaction, *Archives of Computational Methods in Engineering* 20 (3) (2013) 185–238. doi:10.1007/s11831-013-9085-5.
- [46] svFSGe (<https://github.com/StanfordCBCL/svFSGe>) (2024). URL <https://github.com/StanfordCBCL/svFSGe>
- [47] R. Schussnig, D. R. Pacheco, M. Kaltenbacher, T.-P. Fries, Semi-implicit fluid–structure interaction in biomedical applications, *Computer Methods in Applied Mechanics and Engineering* 400 (2022) 115489. doi:10.1016/j.cma.2022.115489.
- [48] P. C. Africa, R. Piersanti, M. Fedele, L. Dede', A. Quarteroni, lifex-fiber: an open tool for myofibers generation in cardiac computational models, *BMC Bioinformatics* 24 (1) (apr 2023). doi:10.1186/s12859-023-05260-w.
- [49] M. A. Fernández, Coupling schemes for incompressible fluid–structure interaction: implicit, semi-implicit and explicit, *SeMA Journal* 55 (1) (2011) 59–108. doi:10.1007/bf03322593.
- [50] U. Küttler, W. A. Wall, Fixed-point fluid–structure interaction solvers with dynamic relaxation, *Computational Mechanics* 43 (1) (2008) 61–72. doi:10.1007/s00466-008-0255-5.
- [51] U. Küttler, *Effiziente lösungsverfahren für fluid-struktur-interaktions-probleme*, Dissertation, Technische Universität München, München (2009).
- [52] J. Degroote, K.-J. Bathe, J. Vierendeels, Performance of a new partitioned procedure versus a monolithic procedure in fluid–structure interaction, *Computers & Structures* 87 (11-12) (2009) 793–801. doi:10.1016/j.compstruc.2008.11.013.
- [53] A. S. Les, S. C. Shadden, C. A. Figueroa, J. M. Park, M. M. Tedesco, R. J. Herfkens, R. L. Dalman, C. A. Taylor, Quantification of hemodynamics in abdominal aortic aneurysms during rest and exercise using magnetic resonance imaging and computational fluid dynamics, *Annals of Biomedical Engineering* 38 (4) (2010) 1288–1313. doi:10.1007/s10439-010-9949-x.
- [54] A. Feintuch, P. Ruengsakulrach, A. Lin, J. Zhang, Y.-Q. Zhou, J. Bishop, L. Davidson, D. Courtman, F. S. Foster, D. A. Steinman, R. M. Henkelman, C. R. Ethier, Hemodynamics in the mouse aortic arch as assessed by mri, ultrasound, and numerical modeling, *American Journal of Physiology-Heart and Circulatory Physiology* 292 (2) (2007) H884–H892. doi:10.1152/ajpheart.00796.2006.

- [55] P. N. Watton, N. A. Hill, M. Heil, A mathematical model for the growth of the abdominal aortic aneurysm, *Biomechanics and Modeling in Mechanobiology* 3 (2) (2004) 98–113. doi:10.1007/s10237-004-0052-9.
- [56] J. D. Humphrey, D. M. Milewicz, G. Tellides, M. A. Schwartz, Dysfunctional mechanosensing in aneurysms, *Science* 344 (6183) (2014) 477–479. doi:10.1126/science.1253026.
- [57] A. B. Ramachandra, S. Sankaran, J. D. Humphrey, A. L. Marsden, Computational simulation of the adaptive capacity of vein grafts in response to increased pressure, *Journal of Biomechanical Engineering* 137 (3) (Mar. 2015). doi:10.1115/1.4029021.
- [58] C. Cyron, J. Humphrey, Vascular homeostasis and the concept of mechanobiological stability, *International Journal of Engineering Science* 85 (2014) 203–223. doi:10.1016/j.ijengsci.2014.08.003.
- [59] M. Latorre, J. D. Humphrey, Mechanobiological stability of biological soft tissues, *Journal of the Mechanics and Physics of Solids* 125 (2019) 298–325. doi:10.1016/j.jmps.2018.12.013.
- [60] T. Spenke, N. Delaissé, J. Degroote, N. Hosters, On the number of subproblem iterations per coupling step in partitioned fluid-structure interaction simulations, *arXiv* (Mar. 2023). arXiv:2303.08513, doi:10.48550/ARXIV.2303.08513.
- [61] O. Gültekin, H. Dal, G. A. Holzapfel, On the quasi-incompressible finite element analysis of anisotropic hyperelastic materials, *Computational Mechanics* 63 (3) (2018) 443–453. doi:10.1007/s00466-018-1602-9.
- [62] E. Karabelas, G. Haase, W. Plank, C. M. Augustin, Versatile stabilized finite element formulations for nearly and fully incompressible solid mechanics, *Computational Mechanics* 65 (1) (2019) 193–215. doi:10.1007/s00466-019-01760-w.
- [63] E. Burman, P. Hansbo, The edge stabilization method for finite elements in cfd, in: *Numerical Mathematics and Advanced Applications*, Springer Berlin Heidelberg, 2004, pp. 196–203. doi:10.1007/978-3-642-18775-9_17.
- [64] M. W. Gee, C. Förster, W. A. Wall, A computational strategy for prestressing patient-specific biomechanical problems under finite deformation, *International Journal for Numerical Methods in Biomedical Engineering* 26 (1) (2009) 52–72. doi:10.1002/cnm.1236.
- [65] M. K. Rausch, M. Genet, J. D. Humphrey, An augmented iterative method for identifying a stress-free reference configuration in image-based biomechanical modeling, *Journal of Biomechanics* 58 (2017) 227–231. doi:10.1016/j.jbiomech.2017.04.021.
- [66] M. Genet, A relaxed growth modeling framework for controlling growth-induced residual stresses, *Clinical Biomechanics* 70 (2019) 270–277. doi:10.1016/j.clinbiomech.2019.08.015.
- [67] N. Barnafi, F. Regazzoni, D. Riccobelli, Reconstructing relaxed configurations in elastic bodies: Mathematical formulations and numerical methods for cardiac modeling, *Computer Methods in Applied Mechanics and Engineering* 423 (2024) 116845. doi:10.1016/j.cma.2024.116845.
- [68] J. Wu, C. M. Augustin, S. C. Shadden, Reconstructing vascular homeostasis by growth-based prestretch and optimal fiber deposition, *Journal of the Mechanical Behavior of Biomedical Materials* (2020) 104161 doi:10.1016/j.jmbbm.2020.104161.
- [69] J. D. Laubrie, S. J. Mousavi, S. Avril, About prestretch in homogenized constrained mixture models simulating growth and remodeling in patient-specific aortic geometries, *Biomechanics and Modeling in Mechanobiology* 21 (2) (2022) 455–469. doi:10.1007/s10237-021-01544-3.
- [70] A. M. Gebauer, M. R. Pfaller, F. A. Braeu, C. J. Cyron, W. A. Wall, A homogenized constrained mixture model of cardiac growth and remodeling: analyzing mechanobiological stability and reversal, *Biomechanics and Modeling in Mechanobiology* (jul 2023). doi:10.1007/s10237-023-01747-w.
- [71] A. J. Cocciolone, J. Z. Hawes, M. C. Staiculescu, E. O. Johnson, M. Murshed, J. E. Wagenseil, Elastin, arterial mechanics, and cardiovascular disease, *American Journal of Physiology-Heart and Circulatory Physiology* 315 (2) (2018) H189–H205. doi:10.1152/ajpheart.00087.2018.
- [72] J. F. Eberth, N. Popovic, V. C. Gresham, E. Wilson, J. D. Humphrey, Time course of carotid artery growth and remodeling in response to altered pulsatility, *American Journal of Physiology-Heart and Circulatory Physiology* 299 (6) (2010) H1875–H1883. doi:10.1152/ajpheart.00872.2009.
- [73] M. Kalenik, M. Chalecki, P. Wichowski, Real values of local resistance coefficients during water flow through welded polypropylene t-junctions, *Water* 12 (3) (2020) 895. doi:10.3390/w12030895.
- [74] J. F. Eberth, V. C. Gresham, A. K. Reddy, N. Popovic, E. Wilson, J. D. Humphrey, Importance of pulsatility in hypertensive carotid artery growth and remodeling, *Journal of Hypertension* 27 (10) (2009) 2010–2021. doi:10.1097/hjh.0b013e32832e8dc8.
- [75] P. F. Davies, Hemodynamic shear stress and the endothelium in cardiovascular pathophysiology, *Nature Clinical Practice Cardiovascular Medicine* 6 (1) (2008) 16–26. doi:10.1038/ncpcardio1397.
- [76] C. Wang, B. M. Baker, C. S. Chen, M. A. Schwartz, Endothelial cell sensing of flow direction, *Arteriosclerosis, Thrombosis, and Vascular Biology* 33 (9) (2013) 2130–2136. doi:10.1161/atvbaha.113.301826.
- [77] N. Baeyens, M. A. Schwartz, Biomechanics of vascular mechanosensation and remodeling, *Molecular Biology of the Cell* 27 (1) (2016) 7–11. doi:10.1091/mbc.e14-11-1522.
- [78] Y. Mohamied, E. M. Rowland, E. L. Bailey, S. J. Sherwin, M. A. Schwartz, P. D. Weinberg, Change of direction in the biomechanics of atherosclerosis, *Annals of Biomedical Engineering* 43 (1) (2014) 16–25. doi:10.1007/s10439-014-1095-4.